Nascent dendrite branches initiated by a localized burst of Spire-dependent actin polymerization.

Authors: Deirdre Hatton[1,2,3,6], Claire Marquilly[1,2,6], Caitlin Hanrahan[1,2,3], Tiago Ferreira[1,2], Yimiao Ou[1,2], Lauren Cinq-Mars[1,2,3], Will Silkworth[4], Hannah M. Bailey[4], Margot E. Quinlan[4,5], Donald J. van Meyel[1,2*].

Affiliations: [1]Centre for Research in Neuroscience, Department of Neurology and Neurosurgery, McGill University, Montreal, Quebec, H3G 1A4, Canada.

[2]Research Institute of the McGill University Health Centre, Montreal, Quebec, H3G 1A4 Canada

[3]Integrated Program in Neuroscience, McGill University, Montreal, Quebec, H3A 2B4, Canada

[4] Dept. of Chemistry and Biochemistry, University of California Los Angeles, Los Angeles, CA, 90095, USA.

[5]Molecular Biology Institute, University of California Los Angeles, 607 Charles E. Young Drive, Los Angeles, CA 90095, USA

[6] These authors contributed equally.

***Correspondence**: don.vanmeyel@mcgill.ca

Summary

Dendrites form arbors whose size, shape and complexity define how neurons cover their receptive territories. Actin dynamics contribute to growth and remodeling of dendrite arbors. Here we examined how Spire, a conserved actin nucleation factor, promotes formation of new branches in vivo. In live imaging of Drosophila class IV dendritic arborization (c4da) neurons, Spire was observed at new sites of branch initiation, where it assembled new actin polymer in a burst just prior to filopodial outgrowth. For dendrite arborization, Spire required intact structural domains to nucleate actin and target the secretory network, and interacted with Rab11 GTPase, a key regulator of recycling endosomes. Together, these findings support a model in which Spire cooperates with Rab11 to promote new dendrite branches by linking localized actin dynamics with intracellular trafficking of endosomes that deliver lipids and cargoes to fuel protrusive outgrowth of nascent dendrites.

Introduction

Dendrites have distinct tree-like branching patterns that influence the number, strength, and integration of sensory or synaptic inputs into neurons[1-3]. Understanding how dendrites are shaped during development is essential to gain full insight into the construction of neural circuits that underlie animal survival, behaviors, learning, and memory[4]. A major gap remains in our understanding of the spatial and temporal control of cytoskeletal remodeling responsible for dendrite morphogenesis during development[5], though it is known to involve regulation of actin dynamics[6] by specific proteins to nucleate, elongate and remodel actin filaments[7,8]. Furthermore, to cope with their size and complexity, dendrites have specialized arrangements of secretory network organelles for the biogenesis of cargo-carrying vesicles and their transport to the cell surface[9]. Given the importance of actin and the secretory network for dendrite

development and function, it is important to clarify how they are coordinated to initiate new dendrite branches in vivo[5,10].

New dendrite branches arise from actin-rich filopodia that rapidly extend from initiation sites along established branches[10]. Dendrite filopodia are structurally distinct from conventional filopodia, with an unusual network-like cytoskeletal organization characterized by both branched and linear filaments of mixed polarity[11], suggesting involvement of multiple actin regulatory proteins with distinct activities. Few studies have identified specific actin regulators involved in forming new branches[12-17], and none have pinpointed their regulation of actin to the location and timing of nascent branch outgrowth. In Drosophila larvae, dendritic arborization (da) neurons provide an excellent model to study the roles of actin regulators in the development of dendrite arbors in vivo[18-20]. In da neurons, the locations of dendrite filopodia initiation sites are pre-figured by patches of actin polymer[12,16,21], as has been proposed for dendrite filopodia in the mouse brain also[22]. For the large space-filling arbors of class IV da (c4da) neurons, the formation of new dendrites requires the Arp2/3 actin nucleator complex under control of the activator WAVE and the small GTPase Rac1[12]. In c4da neurons, new dendrite formation also involves F-actin severing by Twinstar/Cofilin in the production of "blobs" of pre-assembled actin polymer, which move bidirectionally within dendrites, pause before filopodium outgrowth, and appear to contribute F-actin into the nascent branch[16]. The factors specifying the location and timing of filopodial outgrowth from actin patches and blobs have not been defined.

Here we explored the role of Spire (Spir), a conserved multi-domain actin nucleation factor. We previously showed that knockdown of Spir with RNA interference (RNAi) in cd4da neurons reduced the number of terminal dendrite branches and compromised the ability of these nociceptive neurons to elicit larval escape from noxious stimulus[23]. Spir is known to co-operate with Fmn-family formins, which are also actin nucleators, during Drosophila and mouse

oogenesis. Spir has four WASP homology 2 (WH2)-domains for actin nucleation, a KIND domain for interaction with Fmn-family formins[24-27], a modified FYVE (mFYVE) domain to target vesicles of the secretory network, and a SPIR-box with potential to interact with Rab GTPases[24,28-31], which play roles in vesicle sorting and transport[32,33]. Previous studies showed functional links between Spir and Rab11 in oocytes, in cultured cells, and in vitro[28,31,34,35], and Rab11 has been shown to be required for correct dendrite arborization of c4da neurons[36-38]. Here we show that Spir stimulates a burst of localized actin polymerization just prior to filopodial outgrowth of new dendrite branches and that Spir cooperates with Rab11 for dendrite arborization. Our data supports a model in which Spir and Rab11 link localized actin assembly with the secretory network to deliver lipids and cargoes to nascent dendrites.

Results

Spir is required in c4da neurons for localized F-actin synthesis just prior to outgrowth of new dendrite branches.

Development of Drosophila c4da dendrites begins in embryogenesis and continues in larval stages, with arbors growing in the larval body wall between muscles and epithelial cells[18]. We produced a *GAL4* line inserted in the *spir* locus (*spir*^{GAL4}) and used it to drive the reporter *UAS-mCD8::GFP*. *spir*^{GAL4} was expressed in c4da neurons (marked by ppk-CD4::tdTom) and other sensory neurons in the larval body wall (Fig. 1A), consistent with our previous report[23]. To examine Spir protein expression within c4da neurons, we developed new anti-Spir sera for immunohistochemistry (IHC) (Fig. S1A), and we also introduced an in-frame epitope-tag (smGFP-HA) into the *spir* locus (Fig. S1C, D). Both approaches showed Spir to be expressed in c4da neurons in third instar (L3) larvae.

73 To reveal actin dynamics leading up to the protrusion of dendrite filopodia, we acquired
74 time-lapse movies in second instar (L2) larvae, capturing F-actin (labeled with LifeAct::GFP)
75 within c4da neurons (labeled with ppk-CD4::tdTom). To study how loss of *spir* affects actin
76 accumulation and new branch initiation in c4da neurons, we used the mutant alleles $spir^{1}$ and
77 $spir^{2F}$, which prematurely truncate Spir within the KIND domain (Fig. 1B)[39]. We examined
78 each allele in combination with a deficiency for *spir* ($spir^{Df}$), which has a distinct genetic
79 background. All heteroallelic combinations of these alleles of *spir* are viable, and so with anti-
80 Spir sera we were able to confirm that *spir* mutants lack Spir expression in larval sensory
81 neurons (Fig. S1B), and adult brain lysates (Fig. S1E).

82 We captured movies of developing c4da dendrites in L2 larvae and mapped the
83 appearances of new branches in control animals heterozygous for $spir^{Df}$ (Fig. 1C, D) or $spir^{2F}$/+
84 (Fig. 1F), or in wild-type (+/+, Fig. 1F). In all of these controls LifeAct::GFP was seen in
85 stationary puncta that appeared prior to branch initiation; in wild-type (+/+) approximately half
86 of these puncta appeared *de novo* (Fig. 1C, F) and the other half were pre-formed actin blobs
87 that moved to the site (Fig. 1D), consistent with a previous report[16]. In $spir^{2F}/spir^{Df}$ mutants,
88 however, new branches arose only from pre-formed actin blobs that moved to the initiation site
89 and not from stationary actin puncta produced *de novo* (Fig. 1E, F).

90 In controls where branches initiated from either blobs or stationary puncta,
91 LifeAct::GFP signal at these sites became more intense just prior to branch initiation and then
92 extended into the protruding nascent branchlet (Fig. 1C, D). We quantified this change of
93 intensity in wild-type (+/+) controls, where LifeAct::GFP increased roughly two-fold on
94 average in the 60s prior to outgrowth and remained at this intensity for ≥ 60s (Fig. 1G). In
95 contrast, in $spir^{2F}/spir^{Df}$ mutants the LifeAct::GFP signal in blobs did not increase prior to
96 branch initiation (Fig. 1E, G), indicating that Spir is required for this localized assembly of F-
97 actin just prior to the outgrowth of new dendrite branches.

98

99 **Localization of Spir at nascent branches.**

100 In c4da dendrites, Spir was observed in puncta in dendrite branches near the cell body,
101 but strong labelling from epithelial cells and muscles prevented their detection and
102 quantification in more distal branches (Fig. S1A, C, D). To overcome this, we expressed a
103 *UAS-Spir::GFP* transgene (Fig. 1B) in c4da neurons with *ppk-GAL4,* and characterized the
104 distribution of Spir::GFP (Fig. S1F). In L3 larvae, GFP-labeled puncta were seen in 100% of
105 shafts, 28% of branch points, and 6% of branch tips (Fig. S1G). Consistent with this, most of
106 these GFP-labeled puncta were found along shafts (57%) or at branch points (36%) (Fig. S1G).

107 We next used live imaging to determine if Spir::GFP localized to sites of new branch
108 initiation in L2 larvae. Movies (~1 frame/2 seconds (sec) for >5 minutes (min)) showed a
109 distribution of Spir::GFP (Fig. 2A, B) similar to that of fixed larvae at L3 (Fig. S1F). Some
110 puncta were stationary while others were steadily motile or moved in a saltatory manner with
111 occasional pauses (Fig. S1H). Motile puncta were often smaller and rounder, while stationary
112 puncta were often larger and irregular in shape. Importantly, every nascent branch in controls
113 (+/+, L2) had a punctum stationed precisely at (68%) or near (< 2 μm, 32%) the initiation site
114 prior to outgrowth (Fig. 2C). These puncta arrived from elsewhere (30%, Fig. 2A, D) or were
115 already at that site in the first frame (70%, Fig. 2B, D), and time until branch outgrowth varied
116 (Fig. 2D). Spir::GFP intensity did not typically increase prior to outgrowth but, in some
117 instances (12%), a motile punctum combined with one already stationed at the future initiation
118 site. Spir::GFP at branch initiation sites was stably maintained throughout the process of
119 filopodial outgrowth, stabilization, or retraction, and invaded the filopodia as they grew (Fig.
120 2B).

121

122 **Spir is required for new branch formation.**

123 At the outset of our timelapse movies, the number of terminal dendrites/μm^2 was
124 reduced in *spir*^{2F}/*spir*^{Df} mutants compared to controls and, importantly, so was the number of
125 new branches/μm^2 formed per min during each movie (Fig. 2E). This was also observed in
126 movies of c4da neurons expressing LifeAct::GFP instead of Spir::GFP (Fig. S2A, B). For new
127 branches, growth occurred by saltatory extensions in both controls and *spir*^{2F}/*spir*^{Df} mutants,
128 but there were no differences between them in mean speed of outgrowth, proportion of time
129 spent paused between extensions, or maximum length of protrusion (Fig. S2C-E). For pre-
130 existing branches, the proportion that were static increased in *spir*^{2F}/*spir*^{Df} mutants (Fig. S2F-
131 I), whether LifeAct::GFP was present or not. Together these results confirm that Spir promotes
132 the formation of new branches and contributes to dynamics of pre-existing ones.

133 Consistent with this, we examined the consequences of Spir function for fully formed
134 arbors of c4da neurons at L3 and found that *spir* mutants (*spir*^{1}/*spir*^{Df} or *spir*^{2F}/*spir*^{Df}) had fewer
135 terminal branches than controls (*spir*^{2F}/+) (Fig. 3A, C), and thus shorter total arbor length (Fig.
136 3D). Sholl analysis also showed reduced peaks of maximum branch density (critical value)
137 (Fig. 3B, F). Dendritic field was reduced in some c4da neurons of s*pir*^{2F}/*spir*^{Df} mutants (Fig.
138 3E), and so we repeated the analysis after removing a subset (4/15) of cells with unusually
139 small dendritic fields. As expected, we found that dendritic field was no longer significantly
140 different from controls (Fig. S3A) but the branching deficits were still strongly evident for the
141 number of terminal dendrites, arbor length and critical value (Fig. S3A-D).

142 Importantly, the selective expression of *UAS-spir::GFP* in c4da neurons with *ppk-*
143 *GAL4* (Fig. 3A) fully rescued number of terminal branches in *spir*^{2F}/*spir*^{Df} mutants (Fig. 3C,
144 Fig. S3B), and critical value (Fig. 3B, F, Fig. S3D), demonstrating that Spir acts within c4da
145 neurons to control these features. It did not fully rescue total arbor length (Fig. 3D, Fig S3C),
146 which is not likely to be due to inadequate expression since IHC (Fig. S1F) and western blots
147 (Fig S1E) showed Spir::GFP at higher levels than endogenous Spir. Perhaps additional cell

148 types contribute to total arbor length, such as epithelial cells in the larval body wall where Spir
149 is expressed (Fig. S1A-D). We conclude that Spir acts within c4da neurons to establish the
150 correct number of terminal branches, likely by contributing to filopodial outgrowth necessary
151 for nascent branches.
152
153 **Each domain of Spir is required for dendrite arborization.**
154 We sought to determine the importance of the four identified protein domains of Spir
155 by testing if disruptive mutations in Spir::GFP (Fig. 1B) could rescue the correct numbers of
156 terminal branches in c4da neurons of *spir* mutants. The Y232K mutation is a missense
157 substitution in the KIND domain known to abolish the interaction between Spir and the Fmn-
158 family formin Cappuccino (Capu) in oocytes[25,40]. The ABCD mutation is a series of 4 triple-
159 alanine substitutions in the WH2 domains that greatly diminish the ability of Spir to polymerize
160 F-actin *in vitro*[24]. The ΔSB mutation is a 20 aa deletion of the entire Spir-box domain which
161 has sequence similarity to the Rab effector protein Rabphilin3a suggesting it interacts with Rab
162 GTPases[28]. Finally, the C5,6S mutation involves substitution of serine residues for 2 key
163 cysteines in the so-called modified FYVE (mFYVE) domain. FYVE domains interact in lipid
164 membranes with Phosphatidylinositol 3-phosphate (PtdIns3P), a prominent component of the
165 membranes in the endosomal system[41]. The mFYVE domain in Spir binds less specifically to
166 negatively charged lipids, including PtdIns3P, and is required for Spir's localization to
167 intracellular membranes[29].
168 When expressed in c4da neurons (with *ppk-GAL4)* of $spir^{2F}/spir^{Df}$ mutants, none of
169 these mutations rescued the number of terminal dendrites per neuron (Fig. 4A) or critical value
170 (Fig. 4B, Fig. S4A). This was not due to insufficient supply because none were expressed at
171 lower levels than intact Spir::GFP in western blots of adult head lysates (Fig. 4C, D and Fig.
172 S4B). The Y232K, ABCD, and C5,6S mutations did not obviously affect the punctate

173 distribution of Spir::GFP in static images of c4da arbors in L3 larvae (Fig. S4C), but the ΔSB
174 mutation caused it to accumulate near the cell soma and form a more continuous pattern (Fig.
175 4E). Though this might be explained in part by unusually high expression levels (Fig. 4C, D
176 and Fig. S4B), these results suggest that the SB domain is required for proper localization of
177 Spir within c4da arbors. None of the mutants appear to have dominant-negative activity, since
178 expression in a wild-type (+/+) background caused no significant differences in number of
179 terminal dendrites or total arbor length compared to Spir::GFP (Fig. S5A-E), though the ΔSB
180 mutation trended toward reductions of both parameters. Based on the failure of these four
181 mutations to rescue $spir^{2F}/spir^{Df}$ mutants, we conclude that each domain of Spir contributes to
182 its control of dendrite branching.
183
184 **Spir and Rab11 cooperate for dendrite arborization.**
185 The pattern and motility of Spir::GFP puncta within dendrites of c4da neurons was
186 reminiscent of elements of the secretory network, where Rab GTPases including Rab11 are
187 key regulators of vesicle and cargo trafficking[32]. Rab11 is associated with the trans-Golgi
188 network, post-Golgi, and recycling endosomes[42]. Rab11 has been shown to be required for
189 correct c4da dendrite arborization[36-38], a finding we confirmed with RNAi knockdown of
190 *Rab11* mRNA in c4da neurons (Fig. 5A) which reduced the numbers of terminal dendrites in
191 L3 larvae (Fig. 5B), total arbor length (Fig. 5C), dendritic field (Fig. 5D), and Sholl critical
192 value (Fig. 5E, F) compared to controls (+/+). In contrast, overexpression of Rab11::GFP in
193 c4da neurons was not sufficient to affect the number of terminal dendrites, arbor length, and
194 Sholl critical value at L3 (Fig. S6A, B, D), though the dendritic field was smaller (Fig. S6C).
195 Whether Rab11 is involved in the initiation of new dendrite branches has not been
196 determined. To address this, we mapped the appearance of new branches in movies (~1 frame/2
197 sec for >5 min) of developing c4da dendrites in L2 larvae (Fig. 5G). We began by examining

198 the distribution of Rab11::GFP, the expression of which had no effect on the dynamics of pre-
199 existing branches (Fig. S6E-H). In controls (+/+, L2) we observed Rab11::GFP at (60%) or
200 near (< 3 μm, 40%) the initiation site of each new dendrite branch (Fig. 5H). Some Rab11::GFP
201 puncta were motile within arbors, but for every nascent branch we observed (n=48),
202 Rab11::GFP was already stationed at the initiation site from the beginning of every movie and
203 so we could not determine how long it had been there prior to outgrowth. Depletion of Rab11
204 by RNAi knockdown reduced the total number of terminal branches/μm^2 at L2 (Fig. 5I) and,
205 importantly, severely reduced the number of new branches/μm^2/min in each movie (Fig. 5J),
206 indicating that Rab11 is indeed required for the initiation of new dendrite branches. As in *spir*
207 mutants (Fig. S2F-I), pre-existing branches were also affected by Rab11 knockdown (Fig. S6E-
208 H): the proportion of branches that both extended and retracted was reduced (Fig. S6G), while
209 the proportion of static branches increased (Fig. S6H). Therefore, loss of Rab11 results in fewer
210 new branches and reduced dynamics of existing ones.

211 Since Rab11, like Spir, is required for proper dendrite arborization, is localized to sites
212 of new branches, and is required for their initiation, we wondered how Rab11 and Spir might
213 be related in regulating these processes. We first asked whether expressing excess Spir::GFP
214 could restore dendrite arborization and new branch formation to neurons lacking Rab11. We
215 found that it did not (Fig. 5B-F, I, J). In the converse experiment, Rab11::YFP overexpression
216 did not restore dendrite arborization to *spir* mutants (Fig. S6I-M). Together these findings
217 suggest that Spir and Rab11 do not lie in a simple linear pathway controlling dendrite
218 development, and so we wondered whether Spir and Rab11 might interact and thereby
219 cooperate with one another for dendrite arborization instead.

220 Genetic interaction experiments that examine trans-heterozygotes for mutant alleles of
221 *spir* and *Rab11* can provide evidence that they cooperate in a common molecular pathway.
222 When compared to control heterozygotes for either mutation alone (Fig. 6A) the c4da neurons

223 of trans-heterozygotes showed reduced numbers of terminal branches (Fig. 6B) and arbor
224 length (Fig. 6C), while dendritic field was largely unaffected (Fig. 6D).

225 We next tested whether Spir and Rab11 can physically associate with one another *in*
226 *vivo*, by co-expressing Spir-tdTom (in all neurons, with *nSyb-GAL4*) with either Rab11::GFP,
227 or Capu::GFP (a positive control), or Rab6::GFP (a negative control). From lysates of adult
228 heads, Spir::tdTom co-immunoprecipitated with Rab11::GFP and with Capu::GFP, but not
229 with Rab6::GFP (Fig. 6E). This suggests that Spir could selectively associate with Rab11-
230 containing protein complexes in neurons. Consistent with this, we found that upon
231 simultaneous expression of Rab11::mCherry and Spir::GFP in c4da neurons, they were usually
232 co-localized in the cell body, at dendrite branch points and along dendrite shafts (Fig. 6F-H).

233 Since Spir and Rab11 co-localized extensively in dendrites, we wondered whether the
234 positioning of one might be dependent on the other. Upon Rab11 knockdown, the punctate
235 distribution of Spir::GFP was unaffected at L3 (Fig. S7A, B) and, in live imaging at L2,
236 Spir::GFP was still positioned at (56%) or near (< 2 μm, 44%) each new branch initiation site
237 (n=18, Fig. S7C, D). Therefore, Rab11 did not appear to be required for Spir localization at
238 branch initiation sites, and so we wondered if Spir might be required for Rab11 localization
239 instead. For technical reasons, we were unable to examine either Rab11::GFP or Rab11::YFP
240 in *spir* mutants, and so we studied the marker Sec15::GFP instead. Sec15 is a Rab11 binding
241 protein [43-45] and a component of the exocyst, a Rab effector complex of eight proteins involved
242 in the delivery of material to the plasma membrane [46,47]. Like Rab11::GFP, Sec15::GFP showed
243 punctate, motile expression in dendrite arbors in live imaging at L2, where Sec15::GFP was
244 positioned at (80%) or near (< 1 μm, 20%) each initiation site (n=21 new branches in 8 movies,
245 Fig. S7E,F). Sec15::GFP was observed at initiation sites in rare instances where nascent
246 branches were captured in *spir* mutants (n=2, from 11 movies, Fig. S7G), suggesting Spir is
247 not required for positioning Sec15::GFP.

248 We have found that Spir and Rab11 are both required for the synthesis of new dendrite
249 branches and, furthermore, that they genetically interact in vivo, physically interact in neurons
250 and co-localize in dendrites. Together this data provides strong evidence that Spir and Rab11
251 functionally interact with one another, either directly or indirectly, in a common molecular
252 pathway for dendrite arborization in c4da neurons.
253
254 **Discussion**
255 Spir was identified previously as being regulated by Longitudinals Lacking (Lola), a
256 BTB/POZ transcription factor involved in dendrite development[23] and motor axon guidance[48].
257 However, the mechanisms of Spir function in neuronal development have remained unclear.
258 Our data presented here indicate that Spir stimulates localized assembly of actin in the seconds
259 prior to outgrowth of new dendrite branches, and that Spir function is linked to the GTPase
260 Rab11 in the formation of new branches and the dynamic motility of existing ones. Unlike
261 Spir::GFP which arrived from elsewhere in 30% of new branch initiation events, Rab11::GFP
262 was already at the site from the beginning of every movie, suggesting that, at least in some
263 cases Spir is recruited to a pre-existing site marked by the presence of Rab11. Rab11 has been
264 shown to regulate movement of recycling endosomes toward the plasma membrane[49], and the
265 trafficking of receptors and trans-membrane proteins necessary for neurite outgrowth and
266 remodeling [50,51]. Sec15 is a cofactor for Rab11 and a subunit of the exocyst complex, which
267 mediates the tethering of secretory vesicles to the plasma membrane prior to fusion and has
268 been shown to be required for c4da dendrite growth, maintenance, and regeneration following
269 injury[52,53]. We therefore propose that Spir cooperates with Rab11 to couple actin dynamics
270 with the delivery of lipids and cargoes through the secretory network to the exocyst complex,
271 fueling protrusive outgrowth of nascent dendrites. Consistent with this, Spir function in
272 dendrite arborization required intact domains for actin assembly (KIND, WH2) and for

273 targeting Spir to the secretory network (mFYVE). The Spir-box has potential to mediate
274 interactions with Rab GTPases, and we found that it was essential to control the levels and
275 localization of Spir in dendrites. However, the functional and physical interaction between Spir
276 and Rab11 did not involve their interdependent localization, raising the possibility that other
277 factors are involved in the recruitment of Spir to nascent branch initiation sites within arbors.

278 In control animals, newly formed branches were pre-figured either by the appearance
279 of actin polymer *de novo* or by the arrival of pre-formed actin blobs, in roughly equal
280 proportions. In *spir* mutants, there were fewer new branches, and none stemming from
281 initiation sites with *de novo* actin polymer, indicating that Spir is critical for new dendrite
282 formation from such sites. It is unclear whether stationary actin patches and motile actin blobs
283 are features of convergent or parallel processes to initiate dendrite branches[54]. Although Spir
284 was present and active at initiation sites stemming from pre-formed actin blobs, it was
285 dispensable for branch initiation from at least some of them. From this we infer redundancy
286 with other molecular mechanisms for branch initiation, perhaps involving actin synthesized by
287 the Arp2/3 complex which has been shown to localize transiently to branch initiation sites in
288 c4da neurons[12].

289 Spir::GFP overexpression did not affect dendrite arborization (compare Fig. 3 and Fig.
290 S5), supporting the idea that its expression at nascent branch sites reflects that of endogenous
291 Spir. Since Spir::GFP overexpression was not sufficient to induce ectopic branching, and the
292 interval between stationing of Spir at a branching site and filopodial outgrowth was variable,
293 our findings suggest that Spir activity is tightly regulated and may require additional partners
294 to engage the switch to branch initiation. The KIND domain mutation Y232K is known to
295 abolish the interaction between Spir and the formin Capu, and there is some evidence that Spir
296 and Capu interact for the spike-like protrusions in dendrites of class 3 da neurons[17]. However,
297 in unpublished data we built a $capu^{GAL4}$ line that did not label c4da neurons, and RNAi lines

298 targeting Capu did not reduce terminal branch number when expressed in c4da neurons. Of
299 note, the KIND domain also binds intramolecularly to the mFYVE domain[29], and so perhaps
300 the Y232K and C5,6S mutations in these domains disrupt this interaction and thereby impact
301 Spir function in dendrites. Alternatively, Spir might cooperate with another formin in c4da
302 neurons such as Formin3, which is required for c4da dendrite arborization[55]. Further research
303 will be required to identify a formin partner for Spir in c4da neurons, or to determine if Spir
304 could nucleate actin on its own in neurons, as has been shown *in vitro*[24].

305 Interestingly, the Formin3 ortholog INF2 has been reported to interact with mouse Spir-
306 1 in mammalian cells[56]. Murine orthologs of Spir (Spir-1 and Spir-2) are expressed in the
307 developing CNS and adult brain[57,58]. Decreased Spir-2 expression is associated with epilepsy
308 in humans and mice[59], but it is not known if either Spir-1 or Spir-2 are involved in dendrite
309 arborization in mammals. A distinct actin nucleator known as Cordon-bleu has been
310 demonstrated to promote dendrite branch initiation in cultured hippocampal neurons and slice
311 preparations of cerebellar Purkinje neurons[15].

312 Actin filaments generated by Spir proteins and formins have been shown to provide
313 tracks for myosin-V motors in microtubule-independent transport of Rab11-labeled endosomes
314 to the plasma membrane of oocytes[34,60] and in dispersal of Rab27a-labeled melanosomes in
315 melanocytes[61]. Interestingly, mammalian orthologs of myosin Vb have been shown to bind
316 directly to the orthologs of both Spir and Rab11[35], which together activate myosin Vb and
317 stimulate its motility[31]. In dendrites, Spir could contribute to an actin pool for myosin-V-
318 mediated delivery of Rab11 vesicles to nascent branches, supplying lipids and proteins required
319 for their protrusive growth. This actin pool could allow for the subsequent invasion of
320 microtubules into these nascent branches, perhaps mediated by myosin-6[62] or augmin[63], and
321 the transition to microtubule-dependent long-distance transport of cargo-carrying vesicles.
322 While further experiments are required to fully elucidate the mechanisms of dendrite

branching, our findings show that Spir-mediated actin dynamics link branch initiation with protrusive outgrowth in vivo.

Acknowledgements

This work was supported by the Canadian Institutes of Health Research (FRN137034 to DJvM), National Institutes of Health (R01GM096133 to MEQ), a Ruth L. Kirschstein National Research Service Award (GM007185 to HMB), and studentships from the RI-MUHC and McGill (to DH). The authors thank Greg Emery, Peter McPherson and Martine Girard for advice and sharing reagents, our colleagues Emilie Peco, Eunjoo Cho, Adela Ralbovska, Keith Murai, Sabrina Chierzi and Todd Farmer for helpful suggestions. For technical support, the authors thank Dr. Min Fu and Shi-bo Feng of the RI-MUHC Molecular Imaging Platform, and Tim McLean. Stocks obtained from the Bloomington Drosophila Stock Center (NIH P40OD018537) were used in this study.

Author Contributions:

D.J.v.M and M.E.Q. conceived the project and designed experiments with input from all other authors. D.H., C.M., C.H., T.F., Y.O., L.C-M., W.S., and H.M.B. performed experiments and analyzed all data. D.J.v.M wrote the manuscript with input from all other authors.

Declaration of Interests:

The authors declare no competing interests.

348 **Figure Legends**

349 **Figure 1: Spir is required for localized F-actin synthesis just prior to new branch**
350 **outgrowth.** (A) *spir*^{GAL4}-driven mCD8::GFP in c4da neurons (ppk-CD4::tdTom) including
351 ddaC (arrowhead), and other sensory neurons in an L3 larva. Scale bar=25µm. (B) Diagram
352 showing Spir protein domains (KIND, WH2, SB, and mFYVE), the locations *spir*^{2F} and *spir*^{1}
353 mutations, and the names of the disruptive mutations (Y232K, ABCD, ΔSB, and C5,6S)
354 introduced into Spir::GFP. (C, D) Filmstrips (Supplemental Videos 1 and 2) of new dendrite
355 branch formation in a c4da neuron (ppk-CD4::tdTom) from a control (*spir*^{Df}/+) L2 larva.
356 LifeAct::GFP (driven by *ppk-GAL4*) reveals actin polymer within dendrites. Arrow (in C)
357 points to a punctum of F-actin appearing *de novo*, and arrowheads (in D) point to a pre-existing
358 punctum that moved from its original position (white arrowhead) to the site of branch initiation
359 (green arrowhead). In all instances, LifeAct::GFP signal intensified just prior to branch
360 initiation. Scale bar = 2µm. (E) Filmstrip (Supplemental Video 3) showing new dendrite branch
361 formation in a *spir*^{2F}/*spir*^{Df} larva at L2, where LifeAct::GFP moved to the initiation site but did
362 not intensify prior to outgrowth (arrow). Scale bar = 2µm. (F) Proportion of newly formed
363 terminal branches in L2 larvae that had either *de novo* F-actin or pre-formed F-actin prior to
364 branch initiation in c4da neurons. Graph shows mean ± SEM, comparing controls (+/+, n=50
365 new branches in movies from 11 neurons) with *spir* heterozygotes (*spir*^{2F}/+, n=18 new
366 branches, 8 movies) and *spir* mutants (*spir*^{2F}/*spir*^{Df}, n=8 new branches, 11 movies). (G) Fold
367 change of F-actin intensity (LifeAct:GFP) at branch initiation sites, from 60s before branch
368 formation to 60s afterward, comparing mean ± SEM of controls (black) and *spir* mutants (red).
369

370 **Figure 2: Spir is at initiation sites for new dendrite branches, and is required for their**
371 **formation.** (A, B) Filmstrips (Supplemental Video 5 and Supplemental Video 6) of control
372 (+/+) L2 larva, where Spir::GFP (arrows) was observed to move to the initiation site of a new

373 dendrite branch (A) or was already stationed there at the beginning of the movie (B). Scale bars
374 = 2μm. (C, D) For newly formed dendrite branches, the distance of the closest Spir::GFP puncta
375 from the site of branch initiation was measured (C), and the time from observation of a
376 stationary Spir::GFP punctum at the site to filopodial outgrowth was recorded (D). (E, F)
377 Dendrite parameters from time lapse movies of control (+/+, n=104 new branches, 10 movies),
378 heterozygotes ($spir^{2F}$/+, n=91 new branches, 10 movies) or $spir^{2F}/spir^{Df}$ mutants (n=42 new
379 branches, 15 movies). (E) Terminal branches/μm^2 in first movie frame (ANOVA
380 F(2,32)=12.30, p<0.0001). (F) Number of new branches/μm^2/min in each movie (ANOVA
381 F(2,32) =9.276, p=0.0007).
382
383 **Figure 3: Spir is required for dendrite arborization of c4da neurons.** (A) Dendrite arbors
384 in a *spir* heterozygote control (left), a *spir* mutant (middle), and a *spir* mutant rescued with
385 Spir::GFP (right). (B) Sholl profiles with dotted line indicating critical value for controls
386 ($spir^{2F/+}$). (C-F) Dendrite parameters per neuron in L3 larvae (n=15 for each genotype).
387 Asterisks indicate significant changes compared to $spir^{2F/+}$ heterozygous controls. (C) Total
388 number of terminal dendrites per neuron (ANOVA (F(4, 70) = 11.30, p < 0.0001). (D) Total
389 length of dendrite arbor (mm) (ANOVA F(4, 70) = 15.12, p < 0.0001). (E) Dendritic field
390 (mm^2) (ANOVA (F(4, 70) = 3.352, p = 0.0144). (F) Sholl critical value (ANOVA (F(4, 70) =
391 8.936, p < 0.0001).
392
393 **Figure 4: Structure-function analysis to identify Spir domains required for dendrite**
394 **arborization and Spir localization.** (A-B) Dendrite parameters (L3 larvae) showing rescue of
395 $spir^{2F}/spir^{Df}$ mutants with Spir::GFP, but failure to rescue by domain-specific mutations (n=15
396 for each genotype). (A) Total number of terminal dendrites per neuron (ANOVA (F(5, 83) =
397 2.269, p = 0.0550). (B) Sholl critical value (ANOVA (F(5, 84) = 3.552, p = 0.058). (C) Anti-

398 GFP and anti-Actin western blot analysis from adult head lysates, where transgenes were
399 expressed in all neurons with nSyb-GAL4. Expected size of Spir::GFP is 142 kDa, and
400 endogenous Actin is 42 kDa. (D) Relative band intensities on western blots (n=3) of Spir::GFP
401 constructs (anti-GFP) normalised to anti-Actin. Spir$^{\Delta SB}$::GFP is expressed at significantly
402 higher levels than Spir::GFP (Friedman test (Q (4) = 10.40, p = 0.0053), with Dunn's post-hoc
403 tests). (E) *ppk-GAL4*-driven Spir::GFP or Spir$^{\Delta SB}$::GFP in a *spir* mutant background. White
404 boxes in left panels indicate areas magnified in panels to their right. Scale bar=50µm. Spir::GFP
405 is punctate in dendrites, but Spir$^{\Delta SB}$::GFP accumulates in a continuous pattern in dendrites
406 proximal to the cell soma (white arrowhead).
407
408 **Figure 5. Rab11 is required in c4da neurons for dendrite arborization and new branch**
409 **formation.** (A) Dendrite arbors of c4da neurons in control (+/+) (left) and *ppk-Gal4*-driven
410 Rab11-RNAi (right) L3 larvae. Scale bar=50µm. (C-G) Dendrite arbor parameters in control
411 (+/+, n=10), *ppk-Gal4*-driven Rab11-RNAi (n=10), and *ppk-Gal4*-driven Rab11-RNAi and
412 Spir::GFP (n=12). Asterisks indicate significant changes compared to +/+ controls. (B) Total
413 number of terminal dendrites (ANOVA (F(2,29) = 41.06 p<0.0001). (C) Total length of
414 dendrite arbor (mm) (ANOVA (F(2,29) = 163.6, p<0.0001). (D) Dendritic field (mm^2)
415 (ANOVA (F(2, 29) = 34.00, p<0.0001). (E) Sholl critical value (ANOVA (F(2, 29) = 79.84,
416 p<0.0001) (F) Sholl profiles. (G) Filmstrip (Supplemental Video 7) of control (+/+) L2 larva,
417 where Rab11::GFP (arrows) was observed at the initiation site of a new dendrite branch. Scale
418 bar = 2µm. (H) Distance of the closest Rab11::GFP puncta from the site of branch initiation
419 (n=48) in control (+/+) L2 larvae. (I, J) Dendrite parameters from time lapse movies of control
420 (+mCD8::GFP, n=72 new branches, 10 movies), *ppk-Gal4*-driven Rab11-RNAi (n=6 new
421 branches, 11 movies) or *ppk-Gal4*-driven Rab11-RNAi and Spir::GFP (n=18 new branches, 9

422 movies). (I) Terminal branches/μm^2 in first movie frame (ANOVA F(2,27)=12.41, p=0.0002).
423 (J) Number of new branches/μm^2/min in each movie (ANOVA F(2,27) =14.29, p<0.0001).
424
425 **Figure 6. Spire interacts with Rab11 in c4da neurons.**
426 (A) Dendrite arbors of c4da neurons in *spir*^{2F}/+ heterozygotes (left), *Rab11*^{Bi93} heterozygotes
427 (middle), and trans-heterozygotes for both (right). (B-D) Dendrite arbor parameters in *spir*
428 heterozygotes (*spir*^{2F}/+, n=15), *Rab11* heterozygotes (*Rab11*^{Bi93}/+, n=17), and trans-
429 heterozygotes (*spir*^{2F}/+; *Rab11*^{Bi93}/+, n=15). Asterisks indicate significant changes compared
430 to *spir*^{2F}/+ heterozygous controls (*P<0.05). (B) Total number of terminal dendrites (ANOVA
431 (F(2, 44) = 4.745 p = 0.0136). (C) Total length of dendrite arbor (mm) (ANOVA (F(2, 44) =
432 5.443, p =0.0077). (D) Dendritic field (mm^2) (ANOVA (F2, 44) = 0.8512, p=0.4338). (E)
433 Spir::tdTom co-immunoprecipitates with either Capu::GFP or Rab11::GFP from adult head
434 lysates, but not with Rab6::GFP. In SDS-PAGE gels, GFP-Trap® immunoprecipitates (IP)
435 were run alongside 1% or 3% of initial lysate (as indicated), and replicate immunoblots were
436 probed with antibodies to detect GFP or tdTom. (F-H) *ppk-GAL4*-driven Spir::GFP (green)
437 and Rab11::mCherry (magenta). (F) Boxes indicate regions of a c4da neuron selected for
438 magnified view of the cell body (white arrowhead) and proximal dendrites (G) or distal
439 dendrites (H). There are many instances of co-localization of Spir::GFP and Rab11::mCherry
440 at branch points (e.g., orange arrowheads) and dendrite shafts (e.g., blue arrowheads). Scale
441 bar in F=50µm.
442
443 **Materials and Methods**
444 ***Drosophila* stocks and genetics:** Fly stocks were obtained from the Bloomington
445 Drosophila Stock Centre (*spir*^{1}, *spir*^{2F}, *spir*^{DfExel6046} (referred to as *spir*^{Df}), Mi05646, Mi05737,
446 *UAS-capu::GFP*, *Rab11*^{Bi93}, *w*^{1118}, *UAS-mCD8::GFP*, *UAS-Rab11::GFP*, *UAS-Rab11::YFP,*

447 *UAS-Rab6::GFP*, *UAS-Rab11-dsRNA* (referred to as *UAS-Rab11-RNAi*), *UAS-LifeAct-GFP*.
448 *ppk-GAL4* and *ppkCD4::tdTom* and *ppkCD4::GFP* were gifts from Dr. Yuh-Nung Jan. *UAS-*
449 *Rab11::mCherry* and *UAS-sec15-GFP were* a gift from Dr. Gregory Emery. *nSyb-GAL4* line
450 was created by Dr Julie Simpson, for which we used 2nd chromosome insertions generated by
451 Dr Stefan Thor. To create the lines *UAS-spir::GFP*, *UAS-spir::tdTom*, *UAS-spir*^{Y232K}*::GFP*,
452 *UAS-spir*^{ABCD}*::GFP*, *UAS-spir*$^{\Delta SB}$*::GFP*, *UAS-spir*^{C5,6S}*::GFP*, DNA constructs encoding full-
453 length Spir or each of the 4 mutated versions [24,28,40] were designed to add C-terminal GFP or
454 tdTomato (tdTom) fluorophores. These constructs were subcloned into the vector pMUH, then
455 microinjected by standard procedures (Bestgene, Inc) to target the VK00027 landing site in the
456 *Drosophila* genome with φc31-mediated integration[64]. *spir*^{GAL4} was generated by inserting a
457 so-called Trojan-GAL4 into the *spir* locus[65,66]. pT-GEM(0) a gift from Benjamin White
458 (Addgene plasmid # 62891) was microinjected (Bestgene, Inc) into MiMIC line, Mi05646[65,66].
459 The same plasmid was injected into MiMIC line Mi05737 to generate *capu*^{GAL4}. CRISPR/Cas9-
460 mediated homologous recombination was used to introduce spaghetti-monster GFP-HA
461 (smGFP-HA)[67] into the *spir* locus. To generate Spir-smGFP-HA flies, we used an approach
462 combining dual guide RNA (gRNA) sequences[68] and short homology arms[69]. The CRISPR
463 Optimal Target finder (http://targetfinder.flycrispr.neuro.brown.edu/index.php) was used to
464 select gRNA sequences for the C-terminus of Spir (5'-
465 GTCGGCCCTGGATCTGACGCCCGTC-3') and just after the 3'UTR (5'-
466 GTCGGCAAACTAAAGAACAAGATTC-3'), and these oligonucleotides were cloned into
467 pCFD3-dU6:3gRNA (Addgene plasmid #49410)[70]. Homology sequences on 200 nucleotides
468 (PAM removed) were cloned into a self-linearizable Puc573 vector for homologous
469 recombination[69]. The repair template included smGFP-HA, the endogenous 3'UTR of Spir,
470 and the fluorescent eye reporter 3xP3-dsRed, all flanked by two PiggyBac recombinase sites.
471 Plasmids expressing the gRNAs (100ng/μL) and donor template (250ng/μL) were mixed and

472 micro-injected into nos-Cas95 embryos[71] (BDSC 78782). Progeny were screened via
473 fluorescence for the 3xP3-dsRed reporter, and fly stocks were established. All injections and
474 initial screening were completed by BestGene (Chino Hills, CA). Proper insertion of smGFP
475 was confirmed via genomic PCR (primers 5'-GGGGATTCAACCTGTTCTCCT-3' and 5'-
476 TGTGCAAGTGCGTTCTGAAG-3'), and expression confirmed by western blot.

477 **Antibodies:** To produce anti-Spir antisera, DNA encoding Spir amino acids 565-692
478 were cloned into pGEX-6P-1 to produce an IPTG-inducible C-terminal GST fusion proteins in
479 BL21 cells. The purified GST fusion protein was injected into two rabbits and the serum was
480 extracted according to approved protocols at the Comparative Medicine and Animal
481 Resources Centre (McGill University) and standards established by the Canadian Council on
482 Animal Care. Crude serum (500 µl) was then pre-absorbed by overnight incubation with 500
483 µl L3 larvae (*spir*^{1}/*spir*^{Df}) that had been fixed previously in 4% PFA. Other primary antibodies
484 for IHC were Alexa-647-conjugated goat anti-HRP (1:800, Jackson ImmunoResearch
485 #123605021) and rabbit anti-HA (1:300, Cell Signaling Technology #3724), while the
486 secondary antibody for anti-Spir was Alexa-647-conjugated goat anti-rabbit (1:1000,
487 Invitrogen, #A21244), and for anti-HA IHC it was Alexa-405-conjugated goat anti-rabbit
488 (1:1000, Invitrogen, #A48254). For western blotting, membranes were incubated with mouse
489 anti-GFP (Clontech #632380), rabbit anti-DsRed (Takara #632496, for tdTom detection),
490 mouse anti-Actin (Sigma #A4700) or rabbit anti-Spire (directed at amino acids 565-692). For
491 detection, HRP-conjugated secondary antibodies (anti-mouse and anti-rabbit (both 1:3000,
492 BioRad) were used and revealed with chemiluminescence (Amersham ECL Western Blotting
493 Detection Reagents).

494 **Immunohistochemistry (IHC):** L3 larvae of either sex were dissected in Sorensen
495 phosphate buffer (pH 7.4) and fixed in 4% paraformaldehyde (in Sorensen's buffer) for 10
496 minutes (min) at room temperature. Washes (3X over 20 min) were done with Sorensen's

497 buffer containing 0.2% Triton-X-100 (Sigma). Specimens were then blocked with Sorensen's
498 buffer containing 5% normal goat serum (NGS), incubated at 4°C with primary antibodies
499 overnight, washed as above, then incubated with secondary antibodies for 2 hours at room
500 temperature. Anti-Spir antiserum for immunohistochemistry was directed at amino acids 1-91.
501 Primary and secondary antibodies were diluted in Sorensen's buffer containing 5% NGS. After
502 a final wash as above, specimens were then mounted with SlowFade Diamond Antifade
503 Mountant (Invitrogen) for imaging.

504 **Co-immunoprecipitation (co-IP) and western blotting:** Lysates for co-IPs and
505 western blots were made from adult heads aged 1-5 days after eclosion. For western blots,
506 heads were mechanically crushed using a motorized pestle directly in 2X Laemmli buffer. For
507 co-IPs, 100 heads were cut and collected on dry ice, then mechanically crushed using a
508 motorized pestle in 100ul of lysis buffer containing 50mM Tris pH, 150mM KCl, 1mM MgCl2,
509 1mM EGTA, Roche protease inhibitor cocktail and 10% glycerol. Lysates were treated with
510 10% deoxycholic acid and 10% Triton X-100, then incubated overnight on a Nutator with anti-
511 GFP bound agarose beads (Chromotek GFP-Trap® #gta). Lysates and beads were separated in
512 a centrifuge, washed with a glycerol free buffer, and the complexes on the beads were
513 dissociated directly in Laemmli buffer, then separated using standard SDS-PAGE and wet-
514 transfer procedures.

515 **Imaging:** All imaging and quantification was of ddaC, the dorsal-most c4da neuron,
516 in abdominal segments of the larval body wall. For static images, L3 larvae were dissected and
517 prepared for IHC, or they were squished directly on the slide in 100% glycerol and prepared
518 for imaging of native fluorescence (GFP, tdTom, mCherry, mRFP) within 10 minutes. Static
519 images were taken with an Olympus Fluoview FV-1000/BX63 confocal microscope using
520 either a 20X or 60X oil-immersion objective lens. All time-lapse imaging was done on L2
521 larvae, where eggs were initially collected for 4h on agar plates containing grape juice and

522 yeast. After 24h, hatched larvae of selected genotypes were transferred on a fresh fly food plate
523 to start timing. L2 larvae (65h ± 4h AEL) were mounted in a drop of halocarbon oil in a
524 polydimethylsiloxane (PDMS) microfluid device, and then imaged by live confocal
525 microscopy (Zeiss, Spinning Disk, Inverted Axio Observer Z1) with 63x objective lens, at
526 room temperature with Immersol W (Zeiss) between lens and coverslip. Using Zen software
527 (Zeiss), live imaging of fluorescent proteins GFP and tdTomato was performed for 5 min with
528 5s interval on average. If GFP only, then the interval was 2s on average. Only movies obtained
529 from larvae that were still alive and active after imaging were used for analysis. Each movie
530 was then registered on ImageJ using StackReg plugin before analysis[72].

531 **Quantification of Lifeact::GFP and Spir::GFP localization:** New branches
532 appearing in each movie were identified, and initiation sites were classified as having *de novo*
533 actin polymer if a punctum of LifeAct::GFP intensity appeared at the site and grew in intensity
534 until protrusion of the new branch. Initiation sites had "pre-formed" actin if motile blobs of
535 LifeAct::GFP were observed to arrive prior to branch outgrowth (motile). Instances where a
536 new branch grew from a site where a LifeAct::GFP punctum existed in the first frame of the
537 movie were disregarded because the movie did not capture the origin of the actin punctum.
538 Consistent with a previous report[16], we observed only a single rare instance where a filopodium
539 grew from an initiation site where LifeAct::GFP was not detected. Overall LifeAct::GFP
540 expression in *spir* mutants appeared lower than in controls, consistent with our previous report
541 for Spir knockdown with RNAi[23], but it was certainly sufficient to monitor actin polymer at
542 sites of branch initiation.

543 To measure the association of Spir::GFP labeled punctae to either a dendrite shaft,
544 branch point, or tip, a custom routine was developed to extract this information from images
545 acquired with a 20X objective (2 to 4 images stitched together where necessary using the
546 Pairwise Stitching plugin[73]. From maximum intensity projections (MIP) of 10 c4da neurons

547 (ddaC) labeled for the dendrite marker CD4-tdTom, signal from beyond the cell of interest was
548 cleared manually, the background was subtracted, and a MIP mask created. This mask was then
549 applied to the SpirFL::GFP channel. Pixels outside the mask were cleared. The MIP mask was
550 skeletonized using Fiji's skeletonization plugin[74] to obtain the location of shafts, branch points,
551 and tips. A script from the Neuroantomy update site was then used to determine which
552 Spir::GFP punctae were associated with such skeleton features. When a Spir::GFP punctum
553 was 3 µm or less (snap-to distance) from either a branch point or tip it was assigned to each,
554 respectively. This snap-to distance was selected because from a representative Spir:GFP image,
555 80% of the punctae had a diameter of 3 µm or less. Additionally, no branch points or tips were
556 3 µm or less apart from one another. The number of punctae at branch points and tips was then
557 divided by the total number of branch points and tips, respectively, to obtain the percent of
558 branch points and tips that were occupied by Spir::GFP.

559 **Dendrite morphometry**: For morphometry of c4da neurons (ddaC) at L3, images were
560 acquired at 20X, with 1 image field usually sufficient to capture the entire dendritic field of a
561 neuron. However, in some cases 2 images were stitched together using the Fiji plugin Pairwise
562 Stitching to generate an image of the entire neuron[73]. Maximum intensity projections of
563 confocal z-series image stacks were segmented as described previously[23]. Various Fiji plugins
564 were used to determine branching characteristics of neurons; Sholl Analysis to generate Sholl
565 profiles and extract Sholl related parameters[75], Strahler Analysis to assess the number of
566 terminal dendrites[75,76], and Analyze Skeleton for total arbor length. Dendritic field was
567 determined by fitting a polygon around the segmented neuron on Fiji, and measuring the area
568 inside the shape[77]. For morphometry of ddaC neurons at L2 in time-lapse movies, the number
569 of terminal dendrites/μm^2 was calculated in the first frame of each movie. For the duration of
570 each movie, the number of new branches/μm^2/minute was calculated.

571 **Measuring dendrite dynamics:** Pre-existing dendrites at the beginning of live imaging
572 movies were analyzed for the dynamics of their terminal branches using MTrackJ[78]. Terminal
573 branch length was compared by an observer every frame of each movie. Dendrites that
574 extended, retracted, or did both, or remained static were recorded, and these numbers were
575 expressed as the percentage of the total number of pre-existing dendrites at the beginning of
576 each movie. Newly formed dendrites were tracked similarly, and their protrusive outgrowth
577 was measured, where mean speed was the average of the speeds of growth for each frame
578 (including extensions and pauses) until the branch stopped growing altogether, or retracted, or
579 the movie ended. The proportion of time the branch paused during this period of saltatory
580 outgrowth was calculated, as was the maximum length of its protrusion.
581 **Graphs and Statistics:** Bar graphs and statistics were done using GraphPad Prism v9,
582 and displayed data is expressed as mean ± standard error (SEM). Asterisks indicate the
583 significance of P-values compared to the indicated control group (*P<0.05, **P<0.01,
584 ***P<0.001, ****P<0.0001). For comparisons of more than two conditions, data were tested
585 for normal distribution using D'Agostino & Pearson test and analyzed for statistical
586 significance using one-way ANOVA (multiple groups) and Dunnett's post-hoc tests were
587 performed. For the repeated measures of western blots, Friedman test was applied then Dunn's
588 post-hoc tests. To compare two conditions, Student's t-test (unpaired, two-tailed) was used.
589
590 **Supplemental Information**
591 **Supplemental Figure S1: Spir expression and motility in dendrites** (related to Figure 2).
592 (A, B) IHC co-labeling for endogenous Spir and horseradish peroxidase (HRP) in the body
593 wall of L3 larvae, showing Spir expression in a *spir*^{1}/+ heterozygote (A) but not in a *spir*$^{1/Df}$
594 hemizygous mutant (B). (C, D) IHC to detect HA-tagged Spir in a Spir-smGFP-HA larva,
595 focusing on cell body of a c4da neuron (C), and distal dendrite arbors (D). (E) Anti-Spir western

596 blot of lysates from dissected adult brains, comparing controls with *spir*$^{1/Df}$ mutants and with
597 flies overexpressing Spir::GFP in all neurons with nSyb-Gal4. Expected mass of Spir::GFP is
598 142kDa, while that of Spir is 115kDa. The increased presence of Spir (115 kDa) upon
599 overexpression of Spir::GFP likely arises from proteolytic cleavage of the GFP tag. (F) ppk-
600 Gal4 driven Spir::GFP expression is detected with native GFP fluorescence in a c4da neuron
601 labelled with tdTom in an L3 larva. In A-D and F, labelled c4da neuron cell bodies are marked
602 (white arrowheads), as are puncta in dendrite shafts (blue arrowheads in D), branch points
603 (orange arrowhead in F), and tips (yellow arrowhead F). Scale bars in A-D = 25um, F = 10 um.
604 (G) Locations of Spir::GFP puncta observed in static images of c4da dendrite arbors at L3
605 (n=10 neurons). (H) Greyscale filmstrip (Supplemental Video 4) from a c4da neuron of an L2
606 larva, where the black arrowhead indicates progressive movement of a Spir::GFP-labelled
607 punctum within a dendrite shaft. Scale bar: 5µm. Motile Spir::GFP puncta moved in both
608 anterograde (64%) and retrograde (36%) directions from the cell soma, and sometimes were
609 observed to switch from one to the other. Some puncta appeared to pass one another, while
610 others merged. Motile Spir::GFP particles were found to travel 0.6 um/s on average, and
611 achieved a maximal speed of 1.1 um/s.
612
613 **Supplemental Figure S2: Quantification of dynamics of newly formed and pre-existing**
614 **terminal branches** (related to Figure 2). (A-B) Dendrite parameters from time-lapse movies
615 of c4da neurons (labeled with ppkCD4::tdTom) in L2 larvae expressing LifeAct::GFP driven
616 by *ppk-GAL4.* Graphs show mean ± SEM, comparing controls (+/+, n=11 movies) with *spir*
617 heterozygotes (*spir*^{2F}/+, n=8) and *spir* mutants (*spir*^{2F}/*spir*^{Df}, n=11). Asterisks indicate
618 significant changes compared to +/+ controls. (A) Number of terminal branches per µm^2 of
619 area in first frame of each movie (ANOVA ($F(2, 27) = 4.079$, $p = 0.0283$). (B) Number of new
620 branches/µm^2/min in each movie (ANOVA ($F(2, 27) = 3.265$, $p = 0.0537$). (C-E) Protrusive

621 growth characteristics of nascent branches in controls (+/+, n=14 movies) and *spir* mutants
622 (*spir*^{2F}/*spir*^{Df}, n=7) in L2 larvae expressing LifeAct::GFP driven by *ppk-GAL4*, including mean
623 speed (C, t-test (t(21) = 1.757, p = 0.0951), time paused (D, t-test(t(21) = 0,7025, p = 0.4909),
624 and maximum protrusion length (E, t-test (t(21) = 1.516, p = 0.1459). Graphs show scatter plot
625 for each branch, with mean ± SEM indicated (ns, not significant). (F-I) For branches that were
626 already present in the first frame of each movie, quantification of percentage of pre-existing
627 branches that extended (F, ANOVA (F (2, 62) = 2.482, p=0.0919), retracted (G, ANOVA (F
628 (2, 62) = 0.6473, p=0.5269), extended and retracted in the same movie (H, ANOVA (F (2, 62)
629 = 4.058, p=0.0221) or remained static (I, ANOVA (F (2, 62) = 4.389, p=0.0165). Results in F-
630 I are combined for neurons that expressed LifeAct-GFP and those that did not, since LifeAct-
631 GFP does not affect the number or dynamics of pre-existing branches. Graphs show mean ±
632 SEM, comparing controls (+/+, n=21 movies) with *spir* heterozygotes (*spir*^{2F}/+, n=18) and *spir*
633 mutants (*spir*^{2F}/*spir*^{Df}, n=26).
634
635 **Supplemental Figure S3: Dendrite parameters for c4da neurons in L3 larvae** (related to
636 Figure 3). (A-D) This is the same dataset shown in Fig. 3, except it was adjusted to control for
637 dendritic field size by removing from the analysis four *spir*$^{2F/Df}$ c4da neurons with unusually
638 small arbors (n=11). Asterisks indicate significant changes compared to *spir*^{2F}/+ heterozygous
639 controls. (A) Dendritic field per neuron (mm^2) (ANOVA (F(4, 66) = 1.912, p = 0.1189. (B)
640 Total number of terminal dendrites per neuron (ANOVA (F(4, 66) = 9.328, p < 0.0001). (C)
641 Total length of dendrite arbor per neuron (mm) (ANOVA (F(4,66) = 12.03, p < 0.0001). (D)
642 Sholl critical value (ANOVA (F(4, 66) = 6.914, p = 0.0001).
643
644 **Supplemental Figure S4: Function, expression, and distribution of Spir::GFP bearing**
645 **domain-specific mutations** (related to Figure 4). (A) Sholl profiles for entire c4da neurons

646 labelled with ppk-CD4::tdTom. (B) Anti-GFP western blot from adult heads of animals
647 overexpressing in all neurons either intact Spir::GFP or Spir::GFP bearing domain-specific
648 mutations. One of three replicate blots, this blot is distinct from the one shown in Fig. 4C and
649 is shown in its entirety. The expected molecular weight of Spir::GFP is 142 kDa, and that of
650 GFP is 27 kDa, and so proteolytic cleavage of GFP is not apparent for most constructs. (C)
651 *ppk-GAL4* drives the expression of $Spir^{Y232K}$::GFP or $Spir^{ABCD}$::GFP or $Spir^{C5,6S}$::GFP in a *spir*
652 mutant background. Punctate distribution of Spir::GFP is maintained for each of these
653 mutations. White boxes in left panels indicate areas magnified in panels to their right. Scale
654 bar=50μm.
655
656 **Supplemental Figure S5: Effects of overexpression of Spir domain-specific mutations on**
657 **c4da dendrite arborization in wild-type (+/+) animals** (related to Fig. 4)**.** (A-E) Dendrite
658 parameters (mean ± SEM) in wild-type L3 larvae (+/+) expressing Spir::GFP ("+ Spir"), or
659 Spir:GFP with domain-specific mutations (n=8-10 for each genotype). Asterisks indicate
660 significant changes compared to + Spir controls (white bar). All animals in this study bore ppk-
661 Gal4 and ppk-CD4::tdTom transgenes. (A) Total number of terminal dendrites per neuron
662 (ANOVA $F(4, 40) = 3.141$, $p = 0.0245$). (B) Total length of dendrite arbor per neuron (mm)
663 (ANOVA $F(4, 40) = 1.783$, $p = 0.1513$). (C) Dendritic field per neuron (mm^2) (ANOVA $F(4,$
664 $40) = 1.843$, $p = 0.1397$). (D) Sholl profiles. (E) Sholl critical value (ANOVA $F(4, 40) = 1.716$,
665 $p = 0.1655$).
666
667 **Supplemental Figure S6: Effects of Rab11 on dendrite dynamics at L2 and dendrite**
668 **arborization at L3** (related to Figure 5). (A-D) Dendrite parameters (mean ± SEM) in control
669 L3 larvae (+/+) and ppk-GAL4-driven Rab11::GFP (n=10 for each genotype). Asterisks
670 indicate significant changes compared to controls. (A) Total number of terminal dendrites per

671 neuron (t-test, t(18) = 0.5270 , p = 0.6046). (B) Total length of dendrite arbor per neuron
672 (mm) (t-test, t(18) = 0.0571 , p = 0.9550). (C) Dendritic field per neuron (mm^2) (t-test, t(18) =
673 3,551 , p = 0.0023). (D) Sholl critical value (t-test, t(18) = 0.1905 , p = 0.8510). (E-H) Dendrite
674 parameters from time-lapse movies of c4da neurons (labeled with ppkCD4::tdTom) in L2
675 larvae. Graphs show mean ± SEM, comparing controls expressing mCD8::GFP (n=10 movies)
676 with Rab11-RNAi driven by *ppk-GAL4* (n=11) and Rab11::GFP driven by *ppk-GAL4* (n=10).
677 Asterisks indicate significant changes compared to controls. For branches that were already
678 present in the first frame of each movie, quantification of percentage of pre-existing branches
679 that extended (E, ANOVA (F (2, 28) = 2.301, p = 0.1188), retracted (F, ANOVA (F (2, 28) =
680 0.5551, p = 0.5802), extended and retracted in the same movie (G, ANOVA (F (2, 28) = 8.343,
681 p = 0.0014) or remained static (H, ANOVA (F (2, 28) = 16.50, p<0.0001). (I-M) L3 dendrite
682 parameters (mean ± SEM) in control $spir^{2F/+}$ heterozygotes expressing Rab11::YFP, $spir^{2F/Df}$
683 mutants with or without Rab11::YFP. (n=10 for each genotype). Asterisks indicate significant
684 changes compared to controls ($spir^{2F/+}$ heterozygotes + Rab11::YFP). (I) Total number of
685 terminal dendrites per neuron (ANOVA (F(2, 27) = 16.21, p < 0.0001). (J) Total length of
686 dendrite arbor per neuron (mm) (ANOVA F(2, 27) = 12,10, p = 0.0002). (K) Dendritic field
687 per neuron (mm^2) (ANOVA (F(2, 27) = 4.941, p = 0.0148). (L) Sholl critical value (ANOVA
688 (F(2, 27) = 8.764, p = 0.0012). (M) Sholl profiles.
689
690 **Supplemental Figure S7: Expression, and distribution of Spir::GFP and Sec15::GFP in**
691 **c4da neurons** (related to Figures 5 and 6). (A, B) Distribution of Spir::GFP in c4da neurons
692 of L3 larvae in controls (+/+, A) and upon Rab11 RNAi knockdown in c4da neurons with *ppk-*
693 *Gal4* (B). White boxes in left panels indicate areas magnified in panels to their right. Upon
694 knockdown of Rab11 in c4da neurons, Spir::GFP retained punctate distribution within dendrite
695 arbors. Scale bars=50µm. (C) Filmstrip (Supplemental Video 8) of Rab11 knockdown L2 larva,

696 where Spir::GFP (arrows) was observed at the initiation site of a new dendrite branch. (D) In
697 Rab11 knockdown c4da neurons, the distance of the closest Spir::GFP puncta from the site of
698 branch initiation (n=18). (E) In control (+/+) c4da neurons, the distance of the closest
699 Sec15::GFP puncta from the site of branch initiation (n=21). (F) Filmstrip (Supplemental
700 Video 9) of control (+/+) L2 larva, where Sec15::GFP (arrowhead) pre-exists at the initiation
701 site of a new dendrite branch. (G) Filmstrip (Supplemental Video 10) of *spir*$^{2F/Df}$ mutant L2
702 larva, with Sec15::GFP (arrowhead) at a rare branch initiation site.
703
704 **Supplemental Video 1 – corresponding to Fig. 1C.** 1 frame/7.2s.
705 **Supplemental Video 2 - corresponding to Fig. 1D.** 1 frame/4.4s.
706 **Supplemental Video 3 - corresponding to Fig. 1E.** 1 frame/6.5s.
707 **Supplemental Video 4 - corresponding to Supplemental Fig. S1H.** 1 frame/~2s.
708 **Supplemental Video 5 - corresponding to Fig. 2A.** 1 frame/~4s.
709 **Supplemental Video 6 - corresponding to Fig. 2B.** 1 frame/~7s.
710 **Supplemental Video 7 - corresponding to Fig. 5G** 1 frame/~6s.
711 **Supplemental Video 8 - corresponding to Supplemental Fig. S7C.** 1 frame/~7s.
712 **Supplemental Video 9 - corresponding to Supplemental Fig. S7F.** 1 frame/~7s.
713 **Supplemental Video 10 - corresponding to Supplemental Fig. S7G.** 1 frame/~7s.
714
715
716 **References**

717 1. Grueber, W.B., Yang, C.H., Ye, B., and Jan, Y.N. (2005). The development of
718 neuronal morphology in insects. Curr Biol *15*, R730-738.
719 2. London, M., and Hausser, M. (2005). Dendritic computation. Annual review of
720 neuroscience *28*, 503-532.

721 3. Lefebvre, J.L., Sanes, J.R., and Kay, J.N. (2015). Development of dendritic form and
722 function. Annual review of cell and developmental biology *31*, 741-777.
723 10.1146/annurev-cellbio-100913-013020.
724 4. Luo, L. (2021). Architectures of neuronal circuits. Science *373*, eabg7285.
725 10.1126/science.abg7285.
726 5. Lefebvre, J.L. (2021). Molecular mechanisms that mediate dendrite morphogenesis.
727 Curr Top Dev Biol *142*, 233-282. 10.1016/bs.ctdb.2020.12.008.
728 6. Konietzny, A., Bar, J., and Mikhaylova, M. (2017). Dendritic Actin Cytoskeleton:
729 Structure, Functions, and Regulations. Frontiers in cellular neuroscience *11*, 147.
730 10.3389/fncel.2017.00147.
731 7. Siton-Mendelson, O., and Bernheim-Groswasser, A. (2017). Functional Actin
732 Networks under Construction: The Cooperative Action of Actin Nucleation and
733 Elongation Factors. Trends Biochem Sci *42*, 414-430. 10.1016/j.tibs.2017.03.002.
734 8. Rottner, K., Faix, J., Bogdan, S., Linder, S., and Kerkhoff, E. (2017). Actin assembly
735 mechanisms at a glance. J Cell Sci *130*, 3427-3435. 10.1242/jcs.206433.
736 9. Kennedy, M.J., and Hanus, C. (2019). Architecture and Dynamics of the Neuronal
737 Secretory Network. Annual review of cell and developmental biology *35*, 543-566.
738 10.1146/annurev-cellbio-100818-125418.
739 10. Lanoue, V., and Cooper, H.M. (2019). Branching mechanisms shaping dendrite
740 architecture. Dev Biol *451*, 16-24. 10.1016/j.ydbio.2018.12.005.
741 11. Korobova, F., and Svitkina, T. (2010). Molecular architecture of synaptic actin
742 cytoskeleton in hippocampal neurons reveals a mechanism of dendritic spine
743 morphogenesis. Mol Biol Cell *21*, 165-176. E09-07-0596 [pii] 10.1091/mbc.E09-07-
744 0596.

745 12. Sturner, T., Tatarnikova, A., Mueller, J., Schaffran, B., Cuntz, H., Zhang, Y.,
746 Nemethova, M., Bogdan, S., Small, V., and Tavosanis, G. (2019). Transient
747 localization of the Arp2/3 complex initiates neuronal dendrite branching in vivo.
748 Development *146*. 10.1242/dev.171397.
749 13. Zou, W., Dong, X., Broederdorf, T.R., Shen, A., Kramer, D.A., Shi, R., Liang, X.,
750 Miller, D.M., 3rd, Xiang, Y.K., Yasuda, R., et al. (2018). A Dendritic Guidance
751 Receptor Complex Brings Together Distinct Actin Regulators to Drive Efficient F-
752 Actin Assembly and Branching. Developmental cell *45*, 362-375 e363.
753 10.1016/j.devcel.2018.04.008.
754 14. Shi, R., Kramer, D.A., Chen, B., and Shen, K. (2021). A two-step actin
755 polymerization mechanism drives dendrite branching. Neural Dev *16*, 3.
756 10.1186/s13064-021-00154-0.
757 15. Hou, W., Izadi, M., Nemitz, S., Haag, N., Kessels, M.M., and Qualmann, B. (2015).
758 The Actin Nucleator Cobl Is Controlled by Calcium and Calmodulin. PLoS Biol *13*,
759 e1002233. 10.1371/journal.pbio.1002233.
760 16. Nithianandam, V., and Chien, C.T. (2018). Actin blobs prefigure dendrite branching
761 sites. The Journal of cell biology *217*, 3731-3746. 10.1083/jcb.201711136.
762 17. Sturner, T., Ferreira Castro, A., Philipps, M., Cuntz, H., and Tavosanis, G. (2022).
763 The branching code: A model of actin-driven dendrite arborization. Cell reports *39*,
764 110746. 10.1016/j.celrep.2022.110746.
765 18. Grueber, W.B., Jan, L.Y., and Jan, Y.N. (2002). Tiling of the Drosophila epidermis by
766 multidendritic sensory neurons. Development *129*, 2867-2878.
767 19. Medina, P.M., Swick, L.L., Andersen, R., Blalock, Z., and Brenman, J.E. (2006). A
768 novel forward genetic screen for identifying mutations affecting larval neuronal
769 dendrite development in Drosophila melanogaster. Genetics *172*, 2325-2335.

770 20. Nagel, A.C., Apidianakis, Y., Wech, I., Maier, D., Delidakis, C., and Preiss, A.
771 (2000). Neural hyperplasia induced by RNA interference with m4/malpha gene
772 activity. Mechanisms of development *98*, 19-28.
773 21. Andersen, R., Li, Y., Resseguie, M., and Brenman, J.E. (2005). Calcium/calmodulin-
774 dependent protein kinase II alters structural plasticity and cytoskeletal dynamics in
775 Drosophila. J Neurosci *25*, 8878-8888. 25/39/8878 [pii]10.1523/ .2005-05.2005.
776 22. Willig, K.I., Steffens, H., Gregor, C., Herholt, A., Rossner, M.J., and Hell, S.W.
777 (2014). Nanoscopy of filamentous actin in cortical dendrites of a living mouse.
778 Biophys J *106*, L01-03. 10.1016/j.bpj.2013.11.1119.
779 23. Ferreira, T., Ou, Y., Li, S., Giniger, E., and van Meyel, D.J. (2014). Dendrite
780 architecture organized by transcriptional control of the F-actin nucleator Spire.
781 Development *141*, 650-660. 10.1242/dev.099655.
782 24. Quinlan, M.E., Heuser, J.E., Kerkhoff, E., and Mullins, R.D. (2005). Drosophila Spire
783 is an actin nucleation factor. Nature *433*, 382-388. nature03241 [pii]
784 10.1038/nature03241.
785 25. Vizcarra, C.L., Kreutz, B., Rodal, A.A., Toms, A.V., Lu, J., Zheng, W., Quinlan,
786 M.E., and Eck, M.J. (2011). Structure and function of the interacting domains of Spire
787 and Fmn-family formins. Proc Natl Acad Sci U S A *108*, 11884-11889. 1105703108
788 [pii] 10.1073/pnas.1105703108.
789 26. Manseau, L.J., and Schupbach, T. (1989). cappuccino and spire: two unique maternal-
790 effect loci required for both the anteroposterior and dorsoventral patterns of the
791 Drosophila embryo. Genes & development *3*, 1437-1452.
792 27. Pfender, S., Kuznetsov, V., Pleiser, S., Kerkhoff, E., and Schuh, M. (2011). Spire-
793 type actin nucleators cooperate with Formin-2 to drive asymmetric oocyte division.
794 Curr Biol *21*, 955-960. S0960-9822(11)00468-4 [pii] 10.1016/j.cub.2011.04.029.

795 28. Kerkhoff, E., Simpson, J.C., Leberfinger, C.B., Otto, I.M., Doerks, T., Bork, P., Rapp,
796 U.R., Raabe, T., and Pepperkok, R. (2001). The Spir actin organizers are involved in
797 vesicle transport processes. Curr Biol *11*, 1963-1968. S0960-9822(01)00602-9 [pii].
798 29. Tittel, J., Welz, T., Czogalla, A., Dietrich, S., Samol-Wolf, A., Schulte, M., Schwille,
799 P., Weidemann, T., and Kerkhoff, E. (2015). Membrane targeting of the Spir.formin
800 actin nucleator complex requires a sequential handshake of polar interactions. The
801 Journal of biological chemistry *290*, 6428-6444. 10.1074/jbc.M114.602672.
802 30. Quinlan, M.E., Hilgert, S., Bedrossian, A., Mullins, R.D., and Kerkhoff, E. (2007).
803 Regulatory interactions between two actin nucleators, Spire and Cappuccino. The
804 Journal of cell biology *179*, 117-128. jcb.200706196 [pii] 10.1083/jcb.200706196.
805 31. Yao, L.L., Hou, W.D., Liang, Y., Li, X.D., and Ji, H.H. (2024). Spire2 and Rab11a
806 synergistically activate myosin-5b motor function. Biochem Biophys Res Commun
807 *703*, 149653. 10.1016/j.bbrc.2024.149653.
808 32. Kiral, F.R., Kohrs, F.E., Jin, E.J., and Hiesinger, P.R. (2018). Rab GTPases and
809 Membrane Trafficking in Neurodegeneration. Curr Biol *28*, R471-R486.
810 10.1016/j.cub.2018.02.010.
811 33. Welz, T., and Kerkhoff, E. (2023). The role of SPIRE actin nucleators in cellular
812 transport processes. J Cell Sci *136*. 10.1242/jcs.260743.
813 34. Schuh, M. (2011). An actin-dependent mechanism for long-range vesicle transport.
814 Nature cell biology *13*, 1431-1436. 10.1038/ncb2353 ncb2353 [pii].
815 35. Pylypenko, O., Welz, T., Tittel, J., Kollmar, M., Chardon, F., Malherbe, G., Weiss, S.,
816 Michel, C.I., Samol-Wolf, A., Grasskamp, A.T., et al. (2016). Coordinated
817 recruitment of Spir actin nucleators and myosin V motors to Rab11 vesicle
818 membranes. Elife *5*. 10.7554/eLife.17523.

819 36. Kramer, R., Rode, S., and Rumpf, S. (2019). Rab11 is required for neurite pruning
820 and developmental membrane protein degradation in Drosophila sensory neurons.
821 Dev Biol *451*, 68-78. 10.1016/j.ydbio.2019.03.003.
822 37. Lin, T., Kao, H.H., Chou, C.H., Chou, C.Y., Liao, Y.C., and Lee, H.H. (2020). Rab11
823 activation by Ik2 kinase is required for dendrite pruning in Drosophila sensory
824 neurons. PLoS genetics *16*, e1008626. 10.1371/journal.pgen.1008626.
825 38. Mitchell, J.W., Midillioglu, I., Schauer, E., Wang, B., Han, C., and Wildonger, J.
826 (2023). Coordination of Pickpocket ion channel delivery and dendrite growth in
827 Drosophila sensory neurons. PLoS genetics *19*, e1011025.
828 10.1371/journal.pgen.1011025.
829 39. Wellington, A., Emmons, S., James, B., Calley, J., Grover, M., Tolias, P., and
830 Manseau, L. (1999). Spire contains actin binding domains and is related to ascidian
831 posterior end mark-5. Development *126*, 5267-5274.
832 40. Quinlan, M.E. (2013). Direct interaction between two actin nucleators is required in
833 Drosophila oogenesis. Development *140*, 4417-4425. 10.1242/dev.097337.
834 41. Marat, A.L., and Haucke, V. (2016). Phosphatidylinositol 3-phosphates-at the
835 interface between cell signalling and membrane traffic. The EMBO journal *35*, 561-
836 579. 10.15252/embj.201593564.
837 42. Sonnichsen, B., De Renzis, S., Nielsen, E., Rietdorf, J., and Zerial, M. (2000).
838 Distinct membrane domains on endosomes in the recycling pathway visualized by
839 multicolor imaging of Rab4, Rab5, and Rab11. The Journal of cell biology *149*, 901-
840 914.
841 43. Zhang, X.M., Ellis, S., Sriratana, A., Mitchell, C.A., and Rowe, T. (2004). Sec15 is an
842 effector for the Rab11 GTPase in mammalian cells. The Journal of biological
843 chemistry *279*, 43027-43034. 10.1074/jbc.M402264200.

844 44. Wu, S., Mehta, S.Q., Pichaud, F., Bellen, H.J., and Quiocho, F.A. (2005). Sec15
845 interacts with Rab11 via a novel domain and affects Rab11 localization in vivo. Nat
846 Struct Mol Biol *12*, 879-885. 10.1038/nsmb987.
847 45. Assaker, G., Ramel, D., Wculek, S.K., Gonzalez-Gaitan, M., and Emery, G. (2010).
848 Spatial restriction of receptor tyrosine kinase activity through a polarized endocytic
849 cycle controls border cell migration. Proc Natl Acad Sci U S A *107*, 22558-22563.
850 10.1073/pnas.1010795108.
851 46. TerBush, D.R., Maurice, T., Roth, D., and Novick, P. (1996). The Exocyst is a
852 multiprotein complex required for exocytosis in Saccharomyces cerevisiae. The
853 EMBO journal *15*, 6483-6494.
854 47. Wu, H., Rossi, G., and Brennwald, P. (2008). The ghost in the machine: small
855 GTPases as spatial regulators of exocytosis. Trends in cell biology *18*, 397-404.
856 10.1016/j.tcb.2008.06.007.
857 48. Gates, M.A., Kannan, R., and Giniger, E. (2011). A genome-wide analysis reveals
858 that the Drosophila transcription factor Lola promotes axon growth in part by
859 suppressing expression of the actin nucleation factor Spire. Neural Dev *6*, 37. 1749-
860 8104-6-37 [pii]10.118 6/1749-8104-6-37.
861 49. Lasiecka, Z.M., and Winckler, B. (2011). Mechanisms of polarized membrane
862 trafficking in neurons -- focusing in on endosomes. Mol Cell Neurosci *48*, 278-287.
863 10.1016/j.mcn.2011.06.013.
864 50. Park, M., Penick, E.C., Edwards, J.G., Kauer, J.A., and Ehlers, M.D. (2004).
865 Recycling endosomes supply AMPA receptors for LTP. Science *305*, 1972-1975.
866 10.1126/science.1102026 305/5692/1972 [pii].
867 51. Eva, R., Dassie, E., Caswell, P.T., Dick, G., ffrench-Constant, C., Norman, J.C., and
868 Fawcett, J.W. (2010). Rab11 and its effector Rab coupling protein contribute to the

869 trafficking of beta 1 integrins during axon growth in adult dorsal root ganglion
870 neurons and PC12 cells. J Neurosci *30*, 11654-11669. 10.1523/JNEUROSCI.2425-
871 10.2010.
872 52. Swope, R.D., Hertzler, J.I., Stone, M.C., Kothe, G.O., and Rolls, M.M. (2022). The
873 exocyst complex is required for developmental and regenerative neurite growth in
874 vivo. Dev Biol *492*, 1-13. 10.1016/j.ydbio.2022.09.005.
875 53. Peng, Y., Lee, J., Rowland, K., Wen, Y., Hua, H., Carlson, N., Lavania, S., Parrish,
876 J.Z., and Kim, M.D. (2015). Regulation of dendrite growth and maintenance by
877 exocytosis. J Cell Sci *128*, 4279-4292. 10.1242/jcs.174771.
878 54. Pai, Y.J., and Moore, A.W. (2018). Dendritic actin delivery service. The Journal of
879 cell biology *217*, 3325-3326. 10.1083/jcb.201808095.
880 55. Das, R., Bhattacharjee, S., Letcher, J.M., Harris, J.M., Nanda, S., Foldi, I., Lottes,
881 E.N., Bobo, H.M., Grantier, B.D., Mihaly, J., et al. (2021). Formin 3 directs dendritic
882 architecture via microtubule regulation and is required for somatosensory nociceptive
883 behavior. Development *148*. 10.1242/dev.187609.
884 56. Manor, U., Bartholomew, S., Golani, G., Christenson, E., Kozlov, M., Higgs, H.,
885 Spudich, J., and Lippincott-Schwartz, J. (2015). A mitochondria-anchored isoform of
886 the actin-nucleating spire protein regulates mitochondrial division. Elife *4*.
887 10.7554/eLife.08828.
888 57. Schumacher, N., Borawski, J.M., Leberfinger, C.B., Gessler, M., and Kerkhoff, E.
889 (2004). Overlapping expression pattern of the actin organizers Spir-1 and formin-2 in
890 the developing mouse nervous system and the adult brain. Gene expression patterns :
891 GEP *4*, 249-255. 10.1016/j.modgep.2003.11.006 S1567133X03002096 [pii].

892 58. Pleiser, S., Rock, R., Wellmann, J., Gessler, M., and Kerkhoff, E. (2010). Expression
893 patterns of the mouse Spir-2 actin nucleator. Gene expression patterns : GEP *10*, 345-
894 350. S1567-133X(10)00080-3 [pii] 10.1016/j.gep.2010.08.001.
895 59. Hao, L., Zhang, H., Peng, X., Yang, Y., Yang, M., Guo, Y., Wang, X., and Jing, W.
896 (2022). Decreased Spire2 Expression is Involved in Epilepsy. Neuroscience *504*, 1-9.
897 10.1016/j.neuroscience.2022.09.008.
898 60. Holubcova, Z., Howard, G., and Schuh, M. (2013). Vesicles modulate an actin
899 network for asymmetric spindle positioning. Nature cell biology *15*, 937-947.
900 10.1038/ncb2802.
901 61. Alzahofi, N., Welz, T., Robinson, C.L., Page, E.L., Briggs, D.A., Stainthorp, A.K.,
902 Reekes, J., Elbe, D.A., Straub, F., Kallemeijn, W.W., et al. (2020). Rab27a co-
903 ordinates actin-dependent transport by controlling organelle-associated motors and
904 track assembly proteins. Nat Commun *11*, 3495. 10.1038/s41467-020-17212-6.
905 62. Yoong, L.F., Lim, H.K., Tran, H., Lackner, S., Zheng, Z., Hong, P., and Moore, A.W.
906 (2020). Atypical Myosin Tunes Dendrite Arbor Subdivision. Neuron *106*, 452-467
907 e458. 10.1016/j.neuron.2020.02.002.
908 63. Zhang, Y., Sung, H.H., Ziegler, A.B., Wu, Y.C., Viais, R., Sanchez-Huertas, C., Kilo,
909 L., Agrican, F.G., Cheng, Y.J., Mouri, K., et al. (2024). Augmin complex activity
910 fine-tunes dendrite morphology through non-centrosomal microtubule nucleation in
911 vivo. J Cell Sci. 10.1242/jcs.261512.
912 64. Pfeiffer, B.D., Ngo, T.T., Hibbard, K.L., Murphy, C., Jenett, A., Truman, J.W., and
913 Rubin, G.M. (2010). Refinement of tools for targeted gene expression in Drosophila.
914 Genetics *186*, 735-755. 10.1534/genetics.110.119917.
915 65. Diao, F., Ironfield, H., Luan, H., Diao, F., Shropshire, W.C., Ewer, J., Marr, E.,
916 Potter, C.J., Landgraf, M., and White, B.H. (2015). Plug-and-play genetic access to

917 drosophila cell types using exchangeable exon cassettes. Cell reports *10*, 1410-1421.
918 10.1016/j.celrep.2015.01.059.
919 66. Venken, K.J., Schulze, K.L., Haelterman, N.A., Pan, H., He, Y., Evans-Holm, M.,
920 Carlson, J.W., Levis, R.W., Spradling, A.C., Hoskins, R.A., and Bellen, H.J. (2011).
921 MiMIC: a highly versatile transposon insertion resource for engineering Drosophila
922 melanogaster genes. Nat Methods *8*, 737-743.
923 67. Viswanathan, S., Williams, M.E., Bloss, E.B., Stasevich, T.J., Speer, C.M., Nern, A.,
924 Pfeiffer, B.D., Hooks, B.M., Li, W.P., English, B.P., et al. (2015). High-performance
925 probes for light and electron microscopy. Nat Methods *12*, 568-576.
926 10.1038/nmeth.3365.
927 68. Bence, M., Jankovics, F., Lukacsovich, T., and Erdelyi, M. (2017). Combining the
928 auxin-inducible degradation system with CRISPR/Cas9-based genome editing for the
929 conditional depletion of endogenous Drosophila melanogaster proteins. The FEBS
930 journal *284*, 1056-1069. 10.1111/febs.14042.
931 69. Kanca, O., Zirin, J., Garcia-Marques, J., Knight, S.M., Yang-Zhou, D., Amador, G.,
932 Chung, H., Zuo, Z., Ma, L., He, Y., et al. (2019). An efficient CRISPR-based strategy
933 to insert small and large fragments of DNA using short homology arms. Elife *8*.
934 10.7554/eLife.51539.
935 70. Port, F., Chen, H.M., Lee, T., and Bullock, S.L. (2014). Optimized CRISPR/Cas tools
936 for efficient germline and somatic genome engineering in Drosophila. Proc Natl Acad
937 Sci U S A *111*, E2967-2976. 10.1073/pnas.1405500111.
938 71. Ren, X., Sun, J., Housden, B.E., Hu, Y., Roesel, C., Lin, S., Liu, L.P., Yang, Z., Mao,
939 D., Sun, L., et al. (2013). Optimized gene editing technology for Drosophila
940 melanogaster using germ line-specific Cas9. Proc Natl Acad Sci U S A *110*, 19012-
941 19017. 10.1073/pnas.1318481110.

942 72. Thevenaz, P., Ruttimann, U.E., and Unser, M. (1998). A pyramid approach to
943 subpixel registration based on intensity. IEEE Trans Image Process *7*, 27-41.
944 10.1109/83.650848.
945 73. Preibisch, S., Saalfeld, S., and Tomancak, P. (2009). Globally optimal stitching of
946 tiled 3D microscopic image acquisitions. Bioinformatics *25*, 1463-1465. btp184 [pii]
947 10.1093/bioinformatics/btp184.
948 74. Arganda-Carreras, I., Fernandez-Gonzalez, R., Munoz-Barrutia, A., and Ortiz-De-
949 Solorzano, C. (2010). 3D reconstruction of histological sections: Application to
950 mammary gland tissue. Microsc Res Tech *73*, 1019-1029. 10.1002/jemt.20829.
951 75. Ferreira, T.A., Blackman, A.V., Oyrer, J., Jayabal, S., Chung, A.J., Watt, A.J.,
952 Sjostrom, P.J., and van Meyel, D.J. (2014). Neuronal morphometry directly from
953 bitmap images. Nat Methods *11*, 982-984. 10.1038/nmeth.3125.
954 76. Strahler, A.N. (1957). Quantitative analysis of watershed geomorphology.
955 Transactions of the American Geophysical Union *38*, 913-920.
956 77. Schindelin, J., Arganda-Carreras, I., Frise, E., Kaynig, V., Longair, M., Pietzsch, T.,
957 Preibisch, S., Rueden, C., Saalfeld, S., Schmid, B., et al. (2012). Fiji: an open-source
958 platform for biological-image analysis. Nat Methods *9*, 676-682. 10.1038/nmeth.2019
959 nmeth.2019 [pii].
960 78. Meijering, E., Dzyubachyk, O., and Smal, I. (2012). Methods for cell and particle
961 tracking. Methods Enzymol *504*, 183-200. 10.1016/B978-0-12-391857-4.00009-4.
962

Figure 1

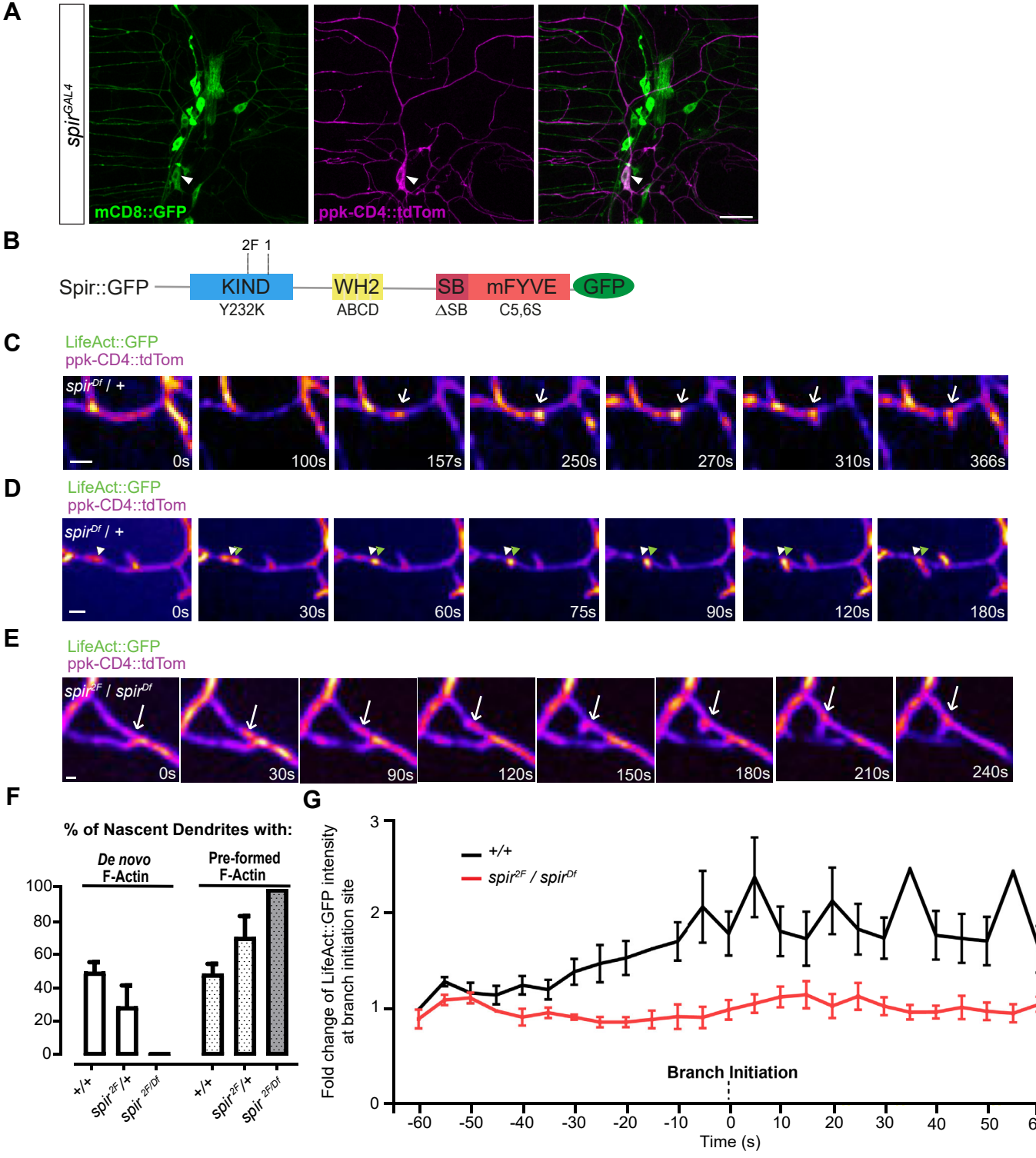
A
spirGAL4
mCD8::GFP
ppk-CD4::tdTom
B
2F 1
Spir::GFP
KIND
Y232K
WH2
ABCD
SB
ΔSB
mFYVE
C5,6S
GFP
C
LifeAct::GFP
ppk-CD4::tdTom
spirDf / +
0s
100s
157s
250s
270s
310s
366s
D
LifeAct::GFP
ppk-CD4::tdTom
spirDf / +
0s
30s
60s
75s
90s
120s
180s
E
LifeAct::GFP
ppk-CD4::tdTom
spir2F / spirDf
0s
30s
90s
120s
150s
180s
210s
240s
F
% of Nascent Dendrites with:
De novo F-Actin
Pre-formed F-Actin
100
80
60
40
20
0
+/+
spir2F/+
spir2F/Df
G
+/+
spir2F / spirDf
Fold change of LifeAct::GFP intensity at branch initiation site
Branch Initiation
Time (s)
-60
-50
-40
-30
-20
-10
0
10
20
30
40
50
60

Figure 2

A Spir::GFP
ppk-CD4::tdTom

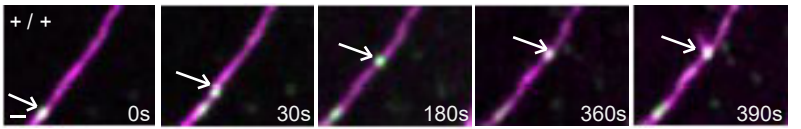

B Spir::GFP
ppk-CD4::tdTom

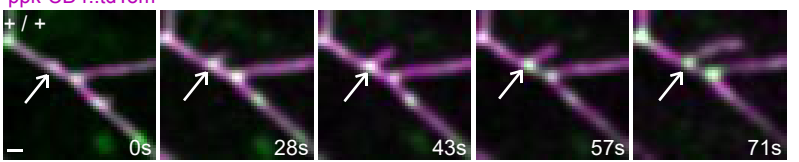

C

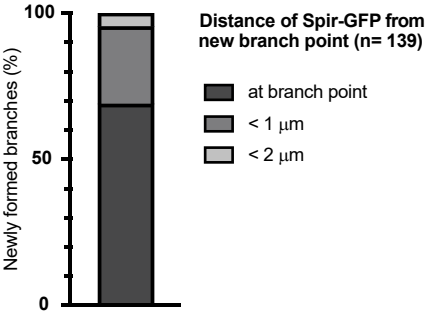

D

Spir::GFP puncta at branch initiation sites in time-lapse movies at L2 (n=61)				
	Occurrence	Time (s) from stationary punctum to branch outgrowth		
		Minimum	Maximum	Mean ±sd
Spir::GFP observed to move to site	30%	4	129	43 ± 41
Spir::GFP stationed at site in first movie frame	70%	8	229	88 ± 67

E

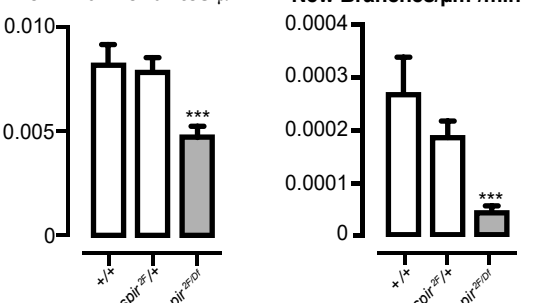

Figure 3

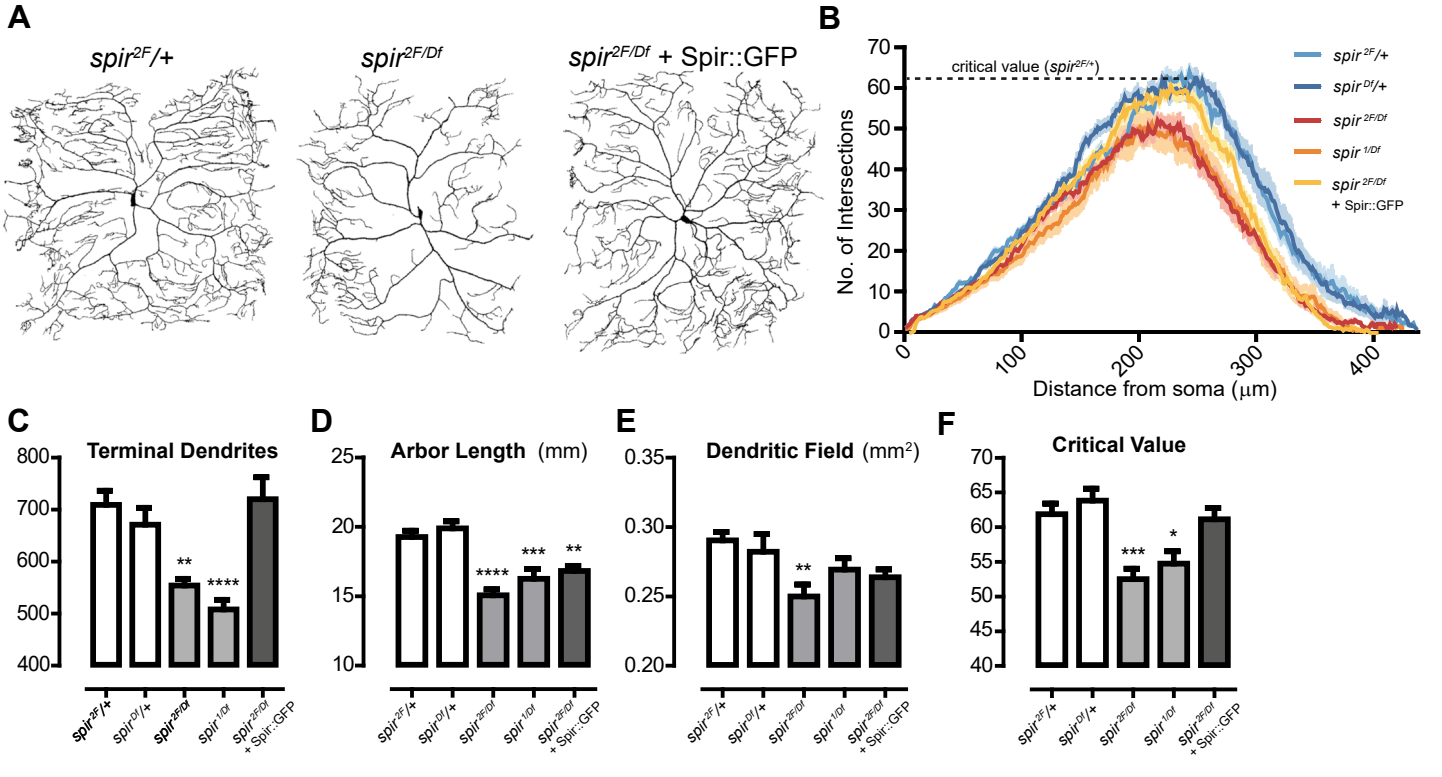
A
spir2F/+
spir2F/Df
spir2F/Df + Spir::GFP
B
critical value (spir2F/+)
No. of Intersections
Distance from soma (μm)
spir 2F/+
spir Df/+
spir 2F/Df
spir 1/Df
spir 2F/Df + Spir::GFP
C
Terminal Dendrites
D
Arbor Length (mm)
E
Dendritic Field (mm2)
F
Critical Value

Figure 4

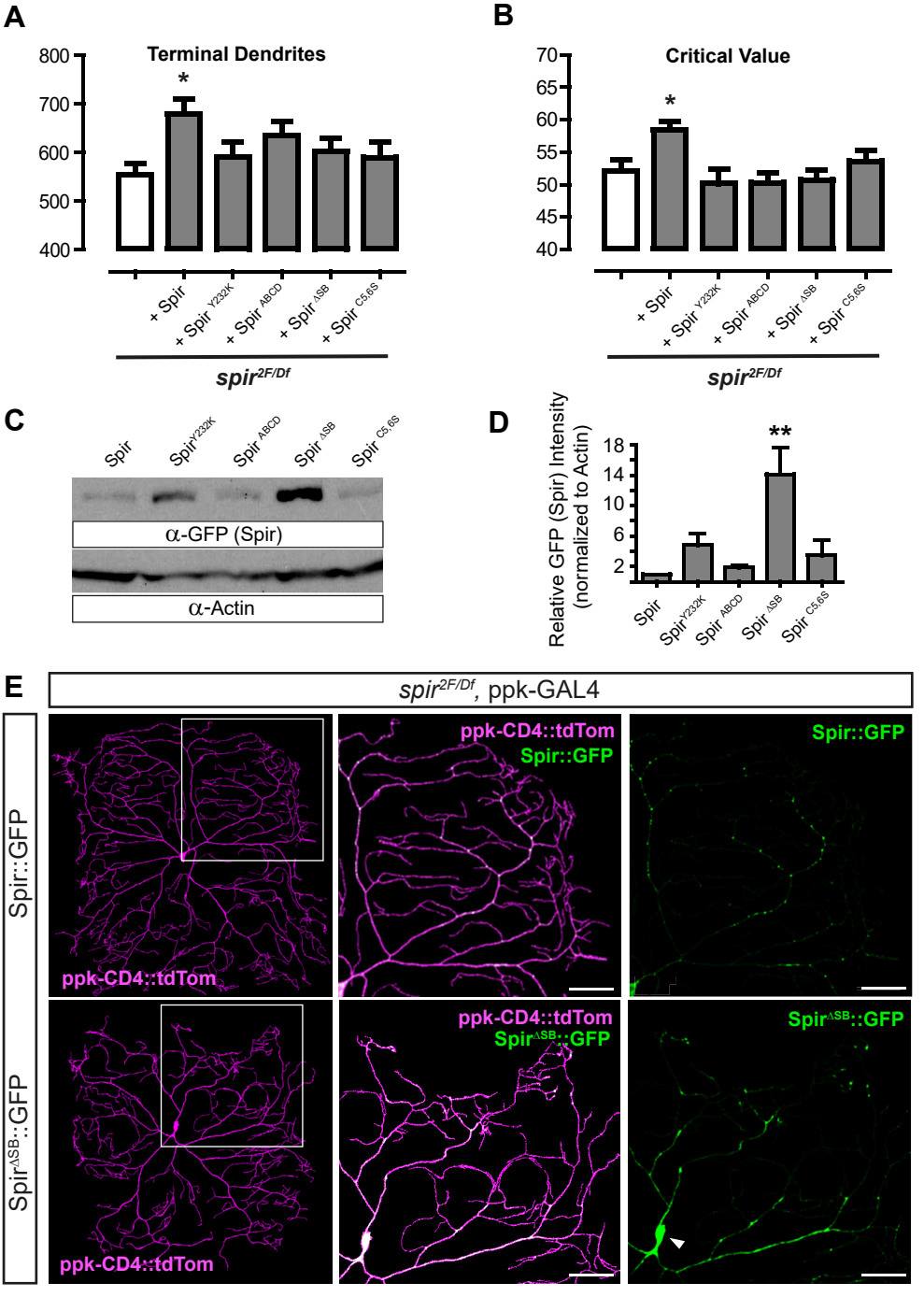
A
Terminal Dendrites
800
700
600
500
400
*
+ Spir
+ Spir Y232K
+ Spir ABCD
+ Spir ΔSB
+ Spir C5,6S
spir2F/Df
B
Critical Value
70
65
60
55
50
45
40
*
+ Spir
+ Spir Y232K
+ Spir ABCD
+ Spir ΔSB
+ Spir C5,6S
spir2F/Df
C
Spir
SpirY232K
Spir ABCD
Spir ΔSB
Spir C5,6S
α-GFP (Spir)
α-Actin
D
Relative GFP (Spir) Intensity (normalized to Actin)
18
14
10
6
2
**
Spir
SpirY232K
Spir ABCD
Spir ΔSB
Spir C5,6S
E
spir2F/Df, ppk-GAL4
Spir::GFP
SpirΔSB::GFP
ppk-CD4::tdTom
ppk-CD4::tdTom
Spir::GFP
Spir::GFP
ppk-CD4::tdTom
ppk-CD4::tdTom
SpirΔSB::GFP
SpirΔSB::GFP

Figure 5

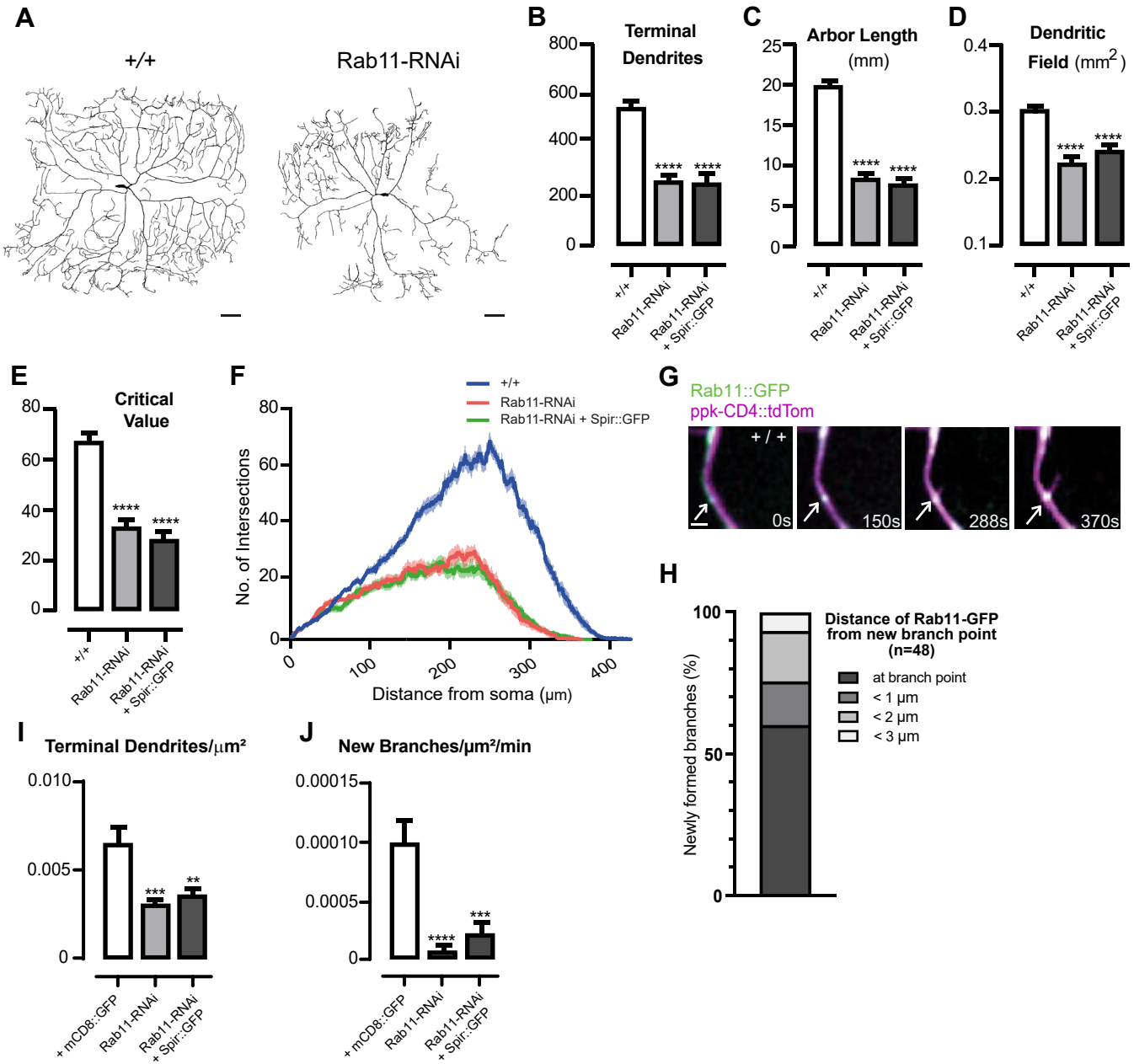
A
+/+
Rab11-RNAi
B
Terminal Dendrites
800
600
400
200
0
****
****
+/+
Rab11-RNAi
Rab11-RNAi + Spir::GFP
C
Arbor Length (mm)
25
20
15
10
5
0
****
****
+/+
Rab11-RNAi
Rab11-RNAi + Spir::GFP
D
Dendritic Field (mm2)
0.4
0.3
0.2
0.1
****
****
+/+
Rab11-RNAi
Rab11-RNAi + Spir::GFP
E
Critical Value
80
60
40
20
0
****
****
+/+
Rab11-RNAi
Rab11-RNAi + Spir::GFP
F
+/+
Rab11-RNAi
Rab11-RNAi + Spir::GFP
No. of Intersections
80
60
40
20
0
0
100
200
300
400
Distance from soma (µm)
G
Rab11::GFP
ppk-CD4::tdTom
+ / +
0s
150s
288s
370s
H
Distance of Rab11-GFP from new branch point (n=48)
at branch point
< 1 µm
< 2 µm
< 3 µm
Newly formed branches (%)
100
50
0
I
Terminal Dendrites/µm²
0.010
0.005
0
***
**
+ mCD8::GFP
Rab11-RNAi
Rab11-RNAi + Spir::GFP
J
New Branches/µm²/min
0.00015
0.00010
0.0005
0
****
***
+ mCD8::GFP
Rab11-RNAi
Rab11-RNAi + Spir::GFP

Figure 6

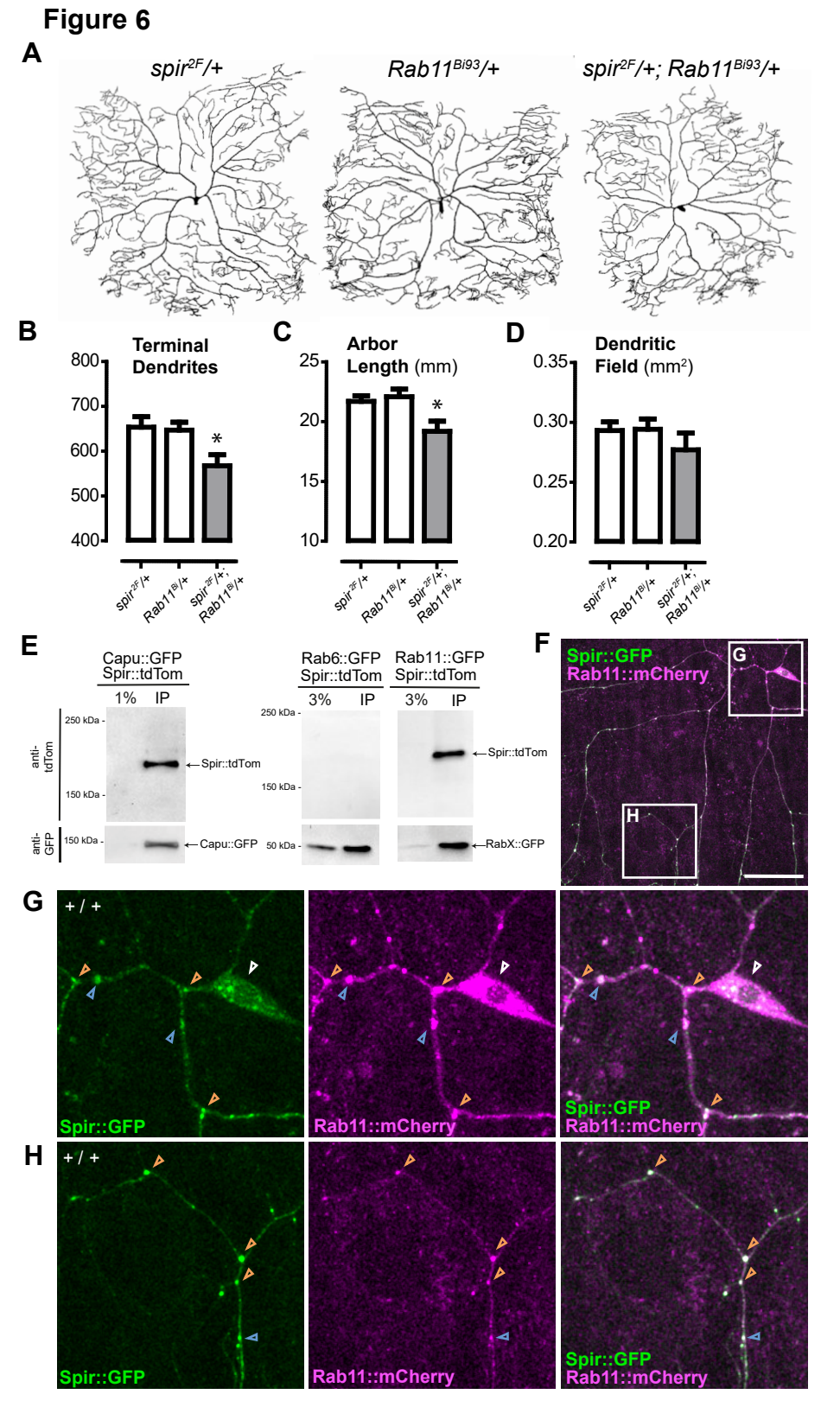
A
spir2F/+
Rab11Bi93/+
spir2F/+; Rab11Bi93/+
B
Terminal Dendrites
800
700
600
500
400
*
spir2F/+
Rab11Bi/+
spir2F/+; Rab11Bi/+
C
Arbor Length (mm)
25
20
15
10
*
D
Dendritic Field (mm2)
0.35
0.30
0.25
0.20
E
Capu::GFP
Spir::tdTom
1%
IP
Rab6::GFP
Spir::tdTom
3%
IP
Rab11::GFP
Spir::tdTom
3%
IP
250 kDa
150 kDa
anti-tdTom
anti-GFP
Spir::tdTom
Capu::GFP
50 kDa
RabX::GFP
F
Spir::GFP
Rab11::mCherry
G
H
+ / +
Spir::GFP
Rab11::mCherry

Figure S1

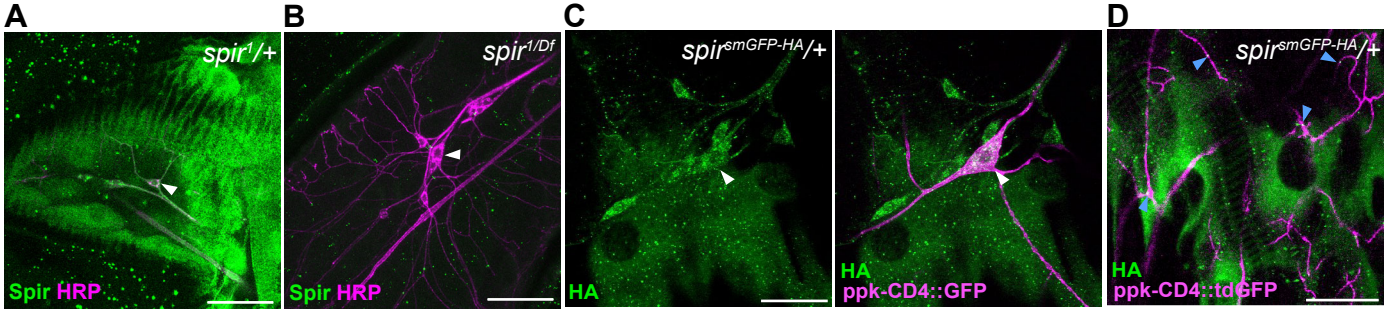

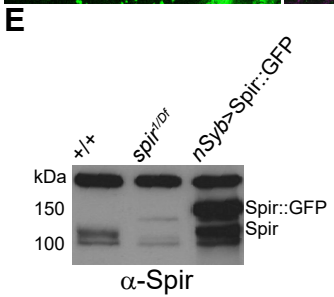

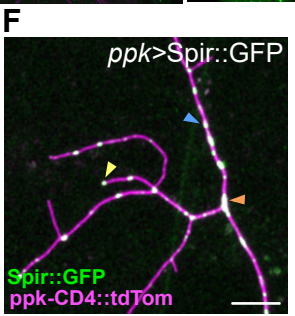

G

Spir::GFP puncta in static images at L3			
	Occurence		
	Shafts	Branch points	Tips
Spir::GFP occupancy of each location	100%	28%	6%
Proportion of total Spir::GFP puncta at each location	57%	36%	7%

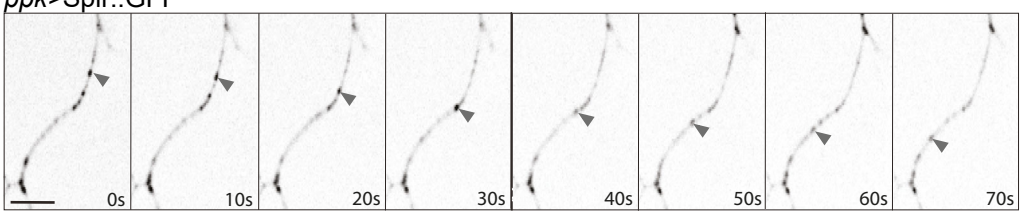

Figure S2

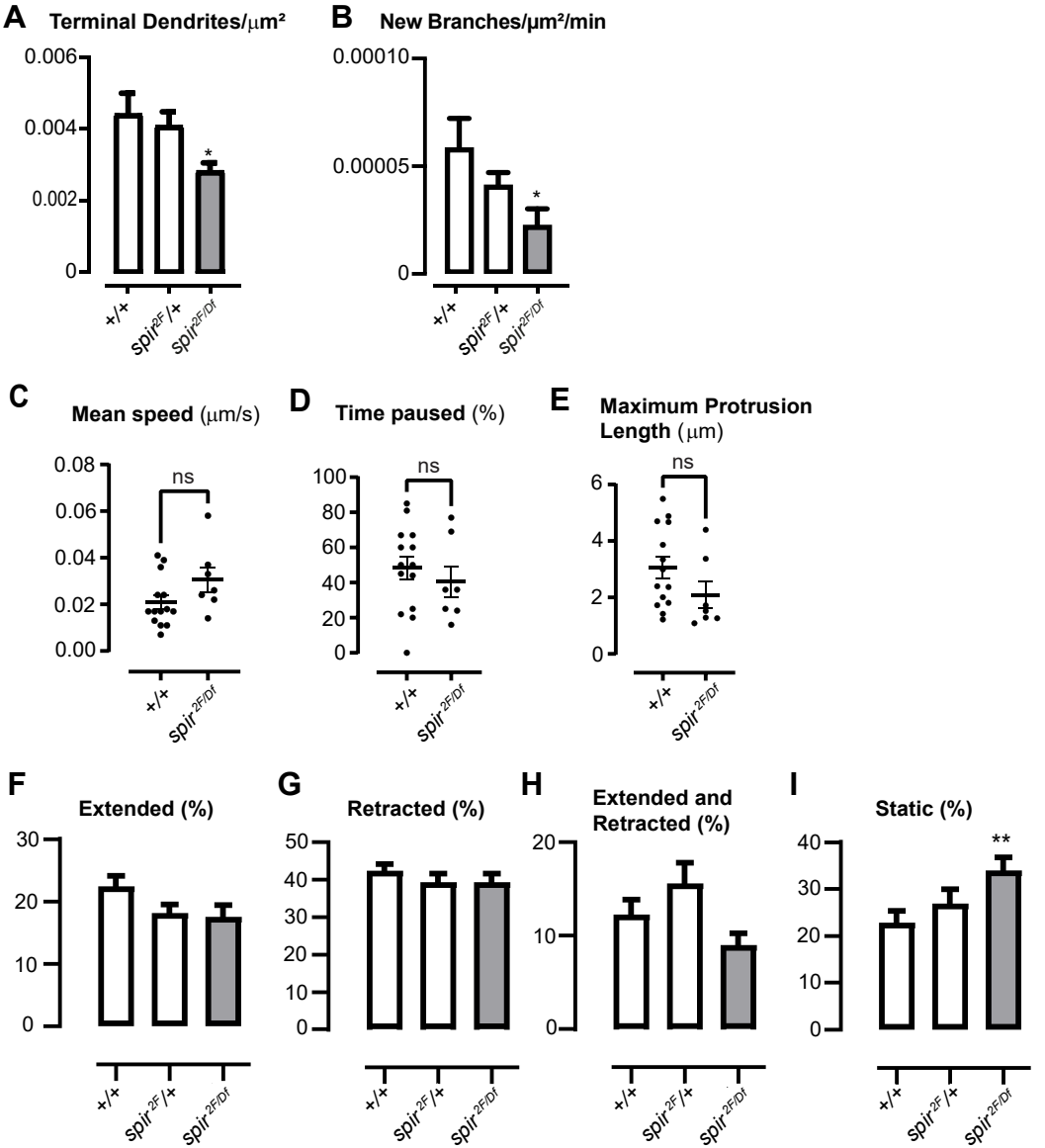
A
Terminal Dendrites/μm²
0.006
0.004
0.002
0
*
+/+
spir2F/+
spir2F/Df
B
New Branches/μm²/min
0.00010
0.00005
0
*
+/+
spir2F/+
spir2F/Df
C
Mean speed (μm/s)
0.08
0.06
0.04
0.02
0.00
ns
+/+
spir2F/Df
D
Time paused (%)
100
80
60
40
20
0
ns
+/+
spir2F/Df
E
Maximum Protrusion Length (μm)
6
4
2
0
ns
+/+
spir2F/Df
F
Extended (%)
30
20
10
0
+/+
spir2F/+
spir2F/Df
G
Retracted (%)
50
40
30
20
10
0
+/+
spir2F/+
spir2F/Df
H
Extended and Retracted (%)
20
10
0
+/+
spir2F/+
spir2F/Df
I
Static (%)
40
30
20
10
0
**
+/+
spir2F/+
spir2F/Df

Figure S3

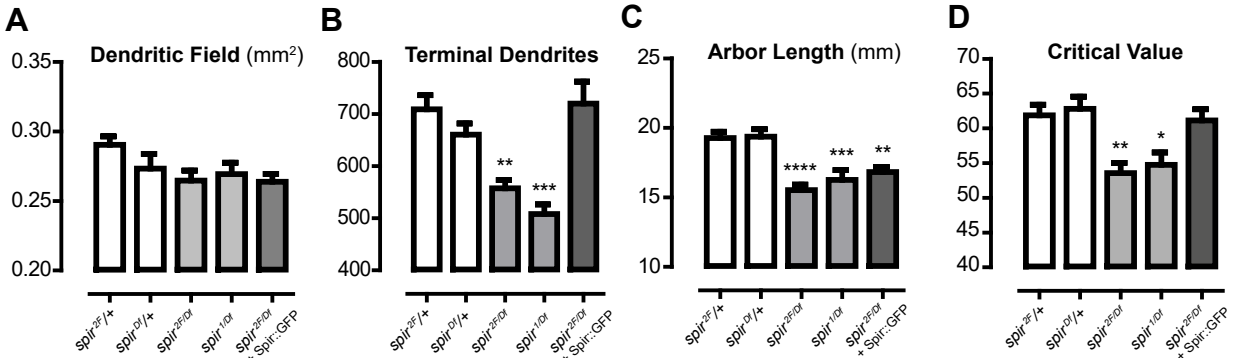
A
Dendritic Field (mm2)
0.35
0.30
0.25
0.20
B
Terminal Dendrites
800
700
600
500
400
**
***
C
Arbor Length (mm)
25
20
15
10
****
***
**
D
Critical Value
70
65
60
55
50
45
40
**
*
spir2F/+
spirD1/+
spir2F/Df
spir1/Df
spir2F/Df + Spir::GFP

Figure S4

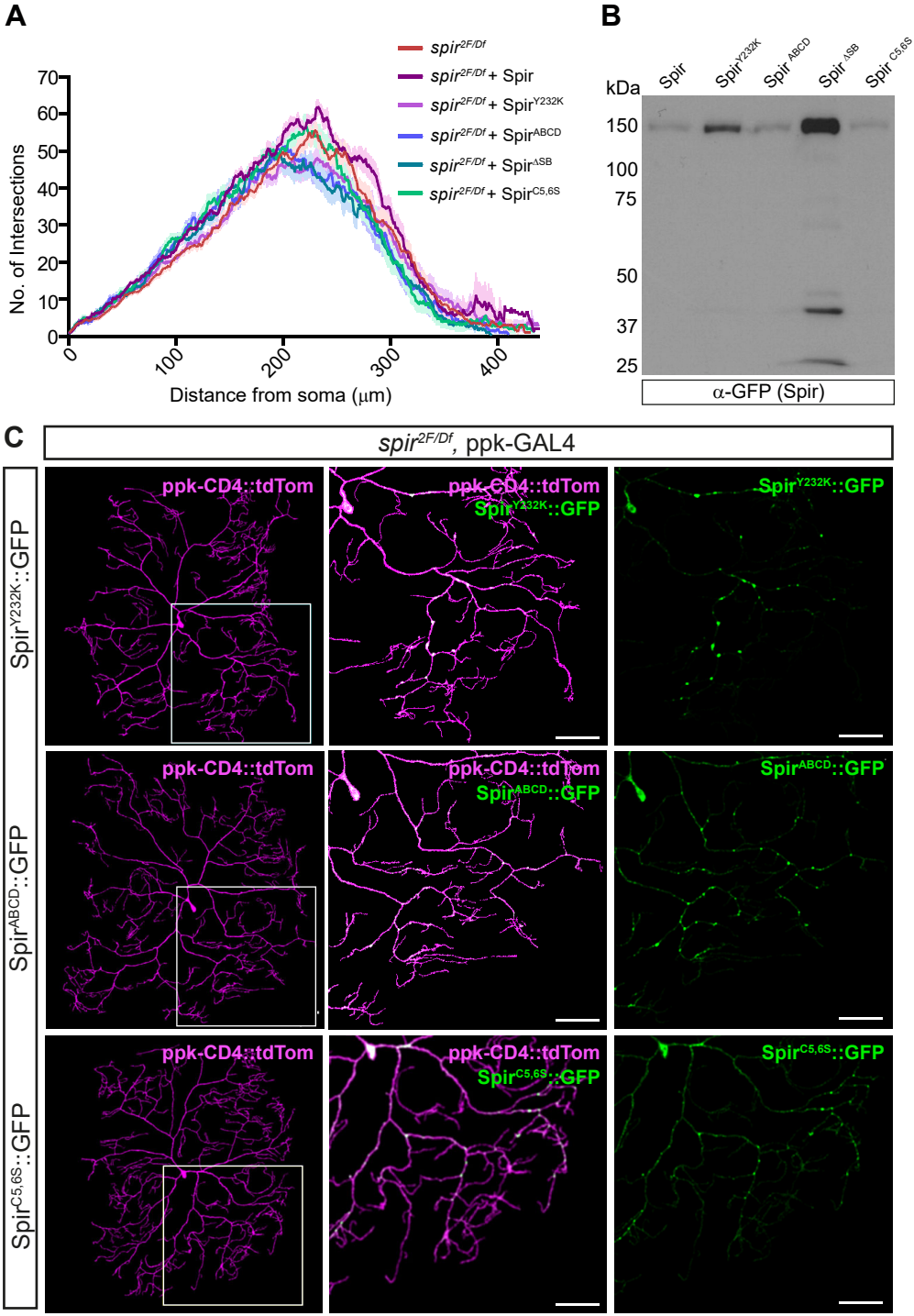
A
spir2F/Df
spir2F/Df + Spir
spir2F/Df + SpirY232K
spir2F/Df + SpirABCD
spir2F/Df + SpirΔSB
spir2F/Df + SpirC5,6S
No. of Intersections
Distance from soma (μm)
B
kDa
Spir
SpirY232K
SpirABCD
SpirΔSB
SpirC5,6S
150
100
75
50
37
25
α-GFP (Spir)
C
spir2F/Df, ppk-GAL4
SpirY232K::GFP
SpirABCD::GFP
SpirC5,6S::GFP
ppk-CD4::tdTom
ppk-CD4::tdTom SpirY232K::GFP
SpirY232K::GFP
ppk-CD4::tdTom SpirABCD::GFP
SpirABCD::GFP
ppk-CD4::tdTom SpirC5,6S::GFP
SpirC5,6S::GFP

Figure S5

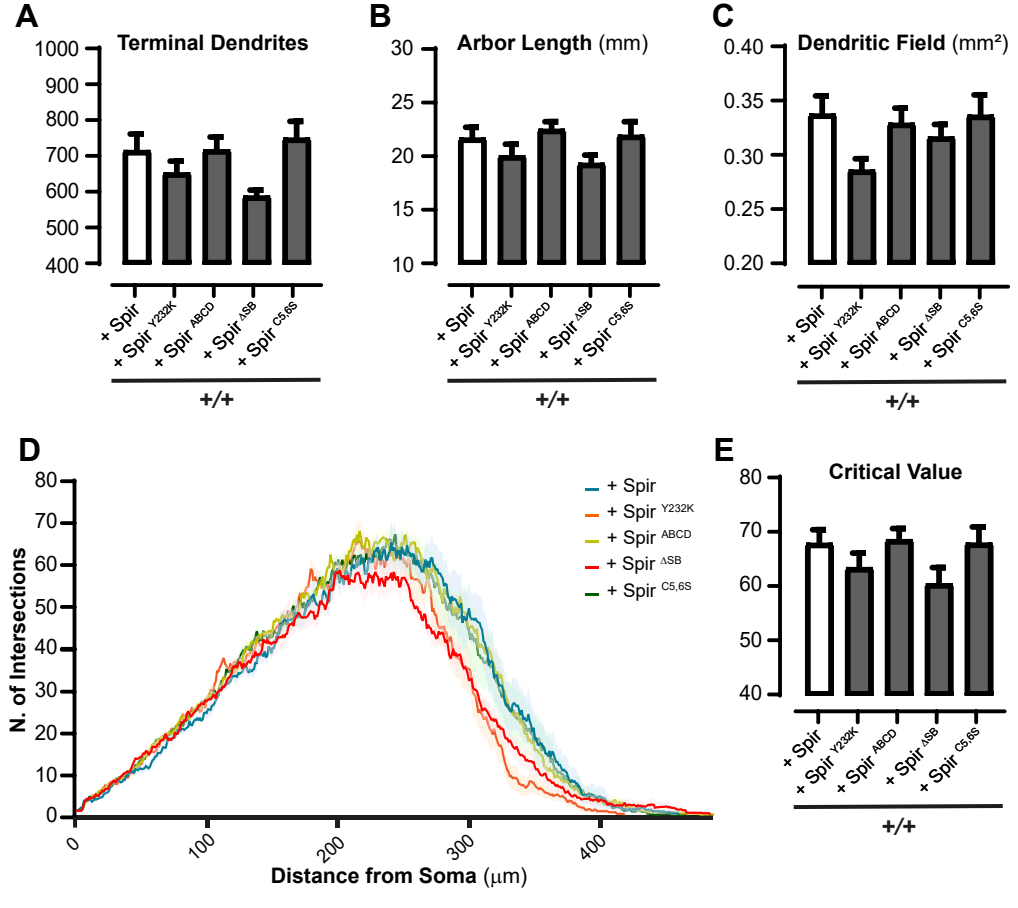
A
Terminal Dendrites
1000
900
800
700
600
500
400
+ Spir
+ Spir Y232K
+ Spir ABCD
+ Spir ΔSB
+ Spir C5,6S
+/+
B
Arbor Length (mm)
30
25
20
15
10
C
Dendritic Field (mm²)
0.40
0.35
0.30
0.25
0.20
D
N. of Intersections
80
70
60
50
40
30
20
10
0
0
100
200
300
400
Distance from Soma (μm)
E
Critical Value

Figure S6

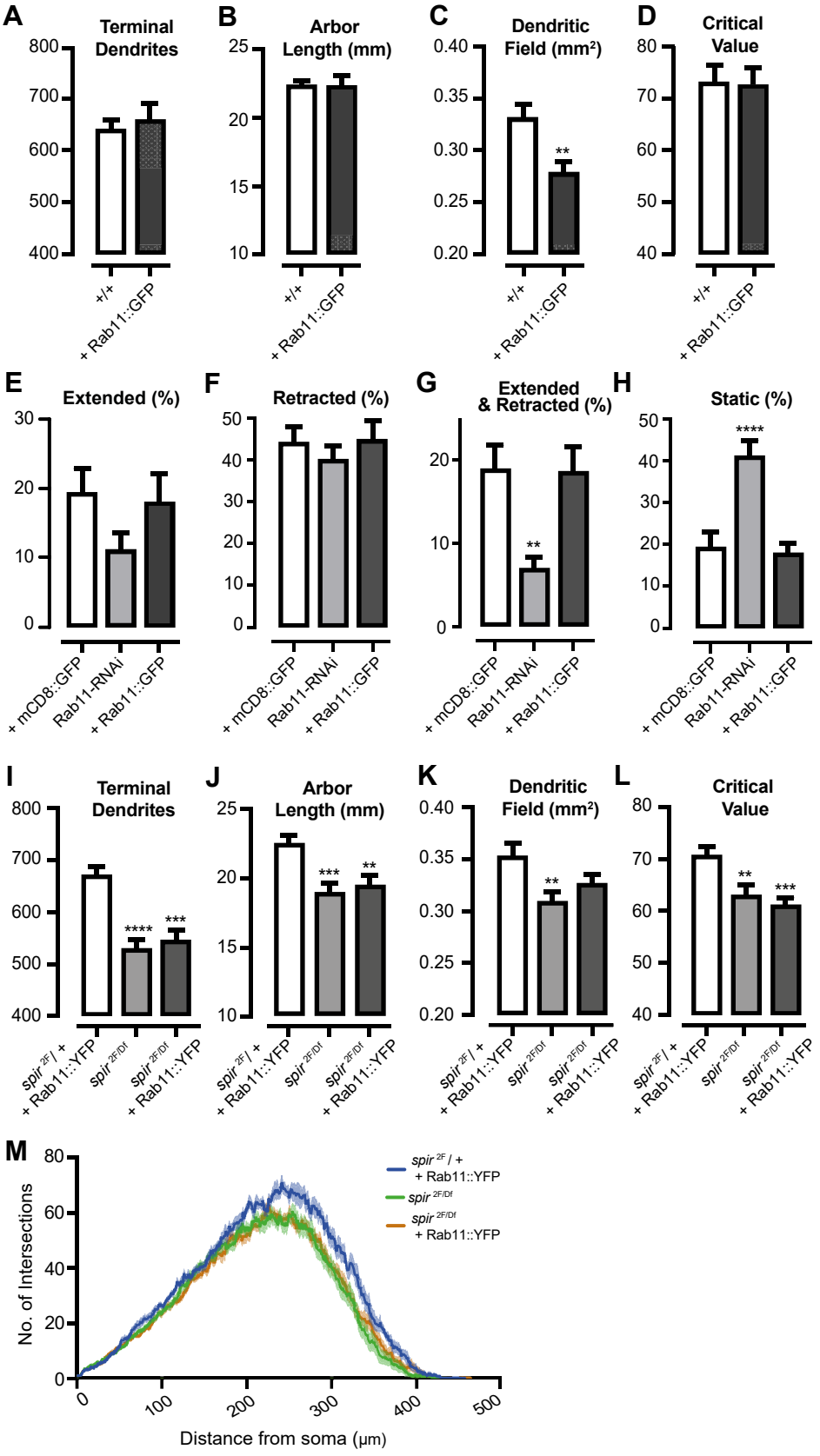
A
Terminal Dendrites
800
700
600
500
400
+/+
+ Rab11::GFP
B
Arbor Length (mm)
25
20
15
10
C
Dendritic Field (mm²)
0.40
0.35
0.30
0.25
0.20
**
D
Critical Value
80
70
60
50
40
E
Extended (%)
30
20
10
0
+ mCD8::GFP
Rab11-RNAi
+ Rab11::GFP
F
Retracted (%)
50
40
30
20
10
0
G
Extended & Retracted (%)
20
10
0
**
H
Static (%)
50
40
30
20
10
0
****
I
Terminal Dendrites
800
700
600
500
400
****
***
spir 2F / +
+ Rab11::YFP
spir 2F/Df
spir 2F/Df
+ Rab11::YFP
J
Arbor Length (mm)
25
20
15
10
***
**
K
Dendritic Field (mm²)
0.40
0.35
0.30
0.25
0.20
**
L
Critical Value
80
70
60
50
40
**
***
M
No. of Intersections
80
60
40
20
0
0
100
200
300
400
500
Distance from soma (μm)
spir 2F / +
+ Rab11::YFP
spir 2F/Df
spir 2F/Df
+ Rab11::YFP

Figure S7

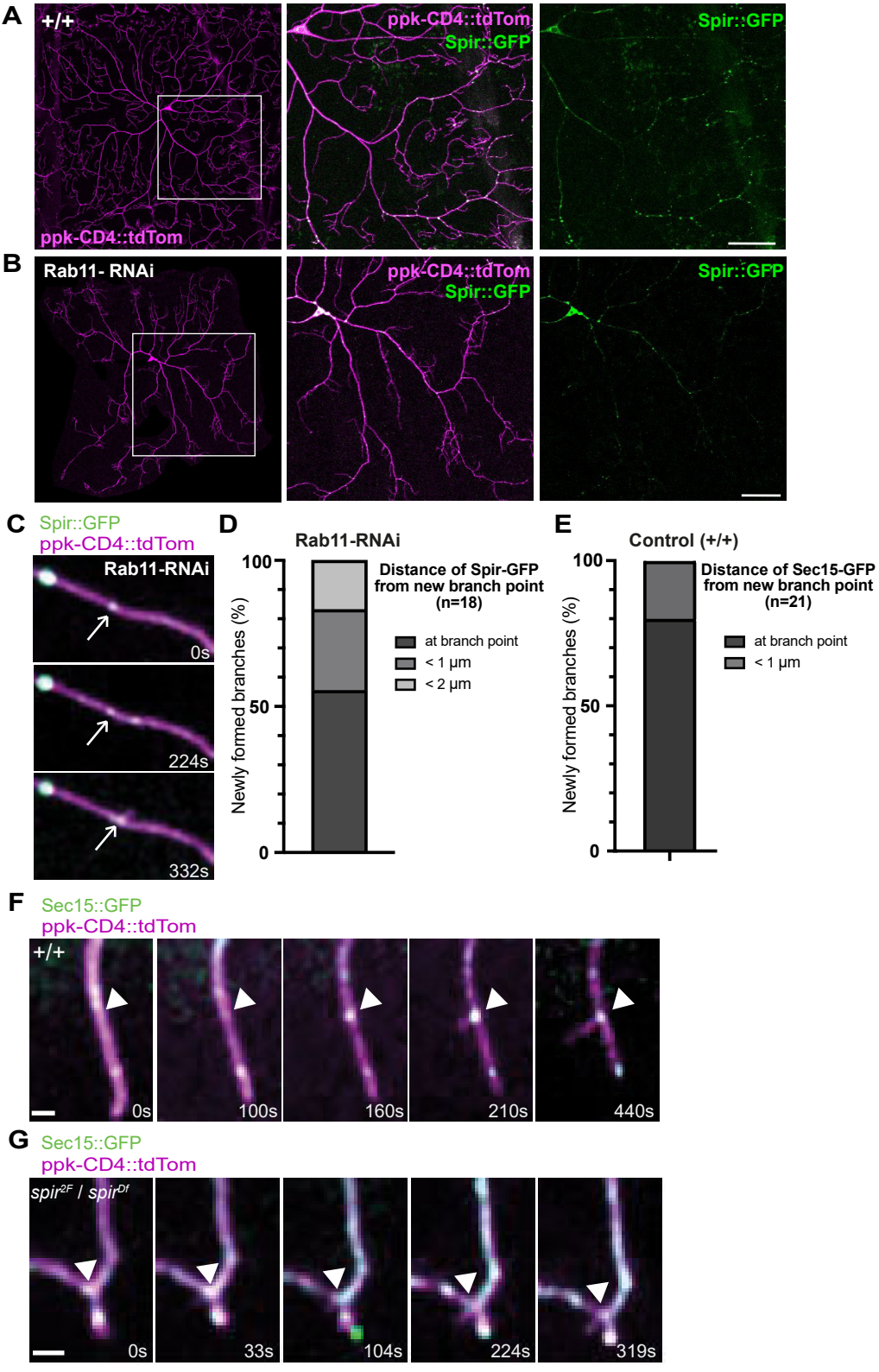
A
+/+
ppk-CD4::tdTom
ppk-CD4::tdTom
Spir::GFP
Spir::GFP
B
Rab11- RNAi
ppk-CD4::tdTom
Spir::GFP
Spir::GFP
C
Spir::GFP
ppk-CD4::tdTom
Rab11-RNAi
0s
224s
332s
D
Rab11-RNAi
Distance of Spir-GFP from new branch point (n=18)
at branch point
< 1 µm
< 2 µm
Newly formed branches (%)
100
50
0
E
Control (+/+)
Distance of Sec15-GFP from new branch point (n=21)
at branch point
< 1 µm
Newly formed branches (%)
100
50
0
F
Sec15::GFP
ppk-CD4::tdTom
+/+
0s
100s
160s
210s
440s
G
Sec15::GFP
ppk-CD4::tdTom
spir2F / spirDf
0s
33s
104s
224s
319s